

Trace the Accretion Geometry of H 1743–322 with Type C Quasi-periodic Oscillations in Multiple Outbursts

QING C. SHUI^{1,2}, S. ZHANG¹, YU P. CHEN¹, SHUANG N. ZHANG^{1,2}, LING D. KONG^{1,3}, PENG J. WANG^{1,2}, L. JI⁴,
HONG X. YIN⁵, JIN L. QU¹, L. TAO¹, MING Y. GE¹, JING Q. PENG^{1,2}, Z. CHANG¹, J. LI^{6,7} AND
P. ZHANG⁸

¹Key Laboratory of Particle Astrophysics, Institute of High Energy Physics, Chinese Academy of Sciences, 100049, Beijing, China

²University of Chinese Academy of Sciences, Chinese Academy of Sciences, 100049, Beijing, China

³Institut für Astronomie und Astrophysik, Kepler Center for Astro and Particle Physics, Eberhard Karls, Universität, Sand 1, D-72076 Tübingen, Germany

⁴School of Physics and Astronomy, Sun Yat-Sen University, Zhuhai, 519082, China

⁵Shandong Key Laboratory of Optical Astronomy and Solar-Terrestrial Environment, School of Space Science and Physics, Institute of Space Sciences, Shandong University, Weihai, Shandong 264209, China

⁶CAS Key Laboratory for Research in Galaxies and Cosmology, Department of Astronomy, University of Science and Technology of China, Hefei 230026, China

⁷School of Astronomy and Space Science, University of Science and Technology of China, Hefei 230026, China

⁸College of Science, China Three Gorges University, Yichang 443002, China

ABSTRACT

We present a systematic analysis of type C quasi-periodic oscillation (QPO) observations of H 1743–322 throughout the *Rossi X-ray Timing Explorer (RXTE)* era. We find that, while different outbursts have significant flux differences, they show consistent positive correlations between the QPO fractional root-mean-square (rms) amplitude and non-thermal fraction of the emission, which indicate an independence of the intrinsic QPO rms on individual outburst brightness in H 1743–322. However, the dependence of the QPO rms on frequency is different between the outburst rise and decay phases, where QPO fractional rms of the decay phase is significantly lower than that of the rise phase at low frequencies. The spectral analysis also reveals different ranges of coronal temperature between the two outburst stages. A semi-quantitative analysis shows that the Lense-Thirring precession model could be responsible for the QPO rms differences, requiring a variable coronal geometric shape. However, the variable-Comptonization model could also account for the findings. The fact that the rms differences and the hysteresis traces in the hardness-intensity diagram (HID) accompany each other indicates a connection between the two phenomena. By correlating the findings with QPO phase lags and the quasi-simultaneous radio flux previously published, we propose there could be corona-jet transitions in H 1743–322 similar to those that have been recently reported in GRS 1915+105.

Keywords: black hole physics – accretion, accretion disc – binaries, close – X-rays: binaries – X-rays: individual (H 1743–322)

1. INTRODUCTION

Undergoing outbursts occasionally after staying with faint luminosity for a long time in quiescence is the primary feature of low mass black hole X-ray binaries (BHXBs) (Remillard & McClintock 2006; Done et al. 2007). Most complete outbursts are observed to have four typical states: the low/hard state (LHS), hard intermediate state (HIMS), soft intermediate state (SIMS) and high soft state (HSS), characterized by different X-ray spectral and variability properties (Belloni et al. 2005; Fender et al. 2009). In the outburst rise phase,

Corresponding author: Qing C. Shui
shuiqc@ihep.ac.cn

Corresponding author: S. Zhang
szhang@ihep.ac.cn

Corresponding author: Yu P. Chen
chenyp@ihep.ac.cn

the system starts from quiescence, increases luminosity with strong variability and non-thermal dominated spectra in the LHS, experiences the hard-to-soft transition in the HIMS and SIMS, and then stays in the HSS with the thermal dominated spectra and weakest variability for weeks. With the decreasing accretion rate, the system goes through the soft-to-hard transition back to the LHS, and fades in quiescence. The different state transition luminosity between the rise and decay phases directly leads to the trace of canonical ‘q’ shape in the hardness-intensity diagram (HID, Homan et al. 2001; Homan & Belloni 2005), and the so-called hysteresis effect which is still not well understood in BHXRBs (Maccarone 2003; Zdziarski et al. 2004; Weng et al. 2021). In addition to these features in the X-ray energy bands, BHXRBs are also characterized by radio/infrared emission, which is generally believed to be associated with relativistic jets (Fender 2001; Fender & Belloni 2004; Méndez et al. 2022, and references therein). In the hard state, radio emission with a flat spectrum ($S_\nu \propto \nu^\alpha$ with $\alpha \sim 0$) is interpreted as self-absorbed synchrotron emission from an optically thick, steady and compact jet (Blandford & Königl 1979; Fender 2001). During the hard-to-soft transition, the steady and compact jet is gradually quenched, where the radio emission, if present, is thought to be attributed to optically thin synchrotron emission from transient ejected plasma clouds with relativistic speeds ($v \sim c$) (Fender et al. 2004).

The X-ray spectrum of a BHXRB usually consists of a thermal and a non-thermal component, the former is believed to come from a geometrically thin and optically thick disc (Shakura & Sunyaev 1973; Lynden-Bell & Pringle 1974), while the latter is produced by the Comptonization of soft photons. However, the geometry of the Comptonizing medium is relatively less clear, which could be an extended cloud consisting of hot electrons (~ 100 keV) called “corona” (Bisnovatyi-Kogan & Blinnikov 1976; Sunyaev & Titarchuk 1980; Titarchuk 1994; Zdziarski et al. 1996, 1999; Życki et al. 1999) or/and the jet-base (Markoff et al. 2005; You et al. 2021). A portion of Comptonized photons can irradiate the disc and then end up as the reflection component which has abundant features, like broad emission lines and Compton hump, etc. (Dauser et al. 2010; García et al. 2014, 2015b, and references therein).

Low frequency quasi-periodic oscillations (LFQPOs, roughly 0.1–30 Hz, van der Klis 1989) are the most prominent features observed in the power density spectrum (PDS) of BHXRBs, with the classification of type A, B and C based on the centroid frequency, quality factor and root-mean-square (rms) amplitude (Wijnands et al. 1999; Casella et al. 2005; Remillard & McClintock 2006).

The appearance of type C QPOs is frequent in the LHS and HIMS with strong amplitudes (fractional rms $\sim 10\%$) and flat-top noise components in the PDS. In the past few decades, several models have been proposed to explain the dynamical origin of QPOs based either on the geometric or the intrinsic properties of the accretion flow. Some examples of the *intrinsic* models are trapped corrugation modes (Kato 1990; Wagoner 1999), the Accretion-ejection instability model (AEI; Tagger & Pellat 1999) and the Two-Component Advection Flow model (TCAF; Molteni et al. 1996), etc.. For the *geometric* models, most of them are related to the relativistic Lense-Thirring (L-T) precession, which was originally invoked to be the dynamic mechanism of QPOs by Stella & Vietri (1998). As an extension of the relativistic precession model (RPM; Stella et al. 1999), the L-T precession model proposed by Ingram et al. (2009) assumes the entire hot flow precesses within the inner radius of the truncated disc (Esin et al. 1997). We refer readers to Ingram & Motta (2019) for recent reviews of observations and theories of LFQPOs.

In addition to the frequency, the radiative properties of QPOs, e.g. rms amplitudes and time lags, etc., also provide extra useful information. Since several observational studies have found that, for most type C QPOs, the variability increases with the photon energy (Zhang et al. 2017; Huang et al. 2018; Kong et al. 2020; Zhang et al. 2020) and no prominent disc-like component exists in the rms spectra (Sobolewska & Życki 2006; Axelsson et al. 2013; Axelsson & Done 2016), the radiative mechanism of the type C QPO should be strongly related to the Comptonized emission. The inclination dependence of amplitudes and time lags (see Motta et al. 2015; van den Eijnden et al. 2017) and reflection variability extracted from the phase-resolved spectroscopy (see Ingram & van der Klis 2015; Ingram et al. 2016, 2017) add support to a geometrical origin, especially the L-T precession model (Ingram et al. 2009). However, these observational findings from different sources show very diverse lacking quantitative explanations, and most recently, Nathan et al. (2022) applied the L-T precession model to fit the phase-resolved spectroscopy of GRS 1915+105 and found an unexpectedly long thermalization time-scale of ~ 70 ms, which is incompatible with the soft lags (~ 1 ms) found in other BHXRBs, e.g. MAXI J1820+070 (Kara et al. 2019) and GX 339–4 (Uttley et al. 2011). These inconsistent findings indicate L-T precession model, especially its radiative part, could be incomplete. Karpouzas et al. (2020) have recently proposed a time-dependent Comptonization model following the work of Lee & Miller (1998) and Kumar & Misra (2014) to quantitatively explain the

energy-dependence of phase lags and rms amplitudes of kilohertz QPOs in neutron-star systems. This model has been successfully applied to BHXRBs, e.g. GRS 1915+105 and MAXI J1348–630 (see Karpouzas et al. 2021; García et al. 2021; Méndez et al. 2022; García et al. 2022). The updated version of the model (Bellavita et al. 2022), incorporating a disc-blackbody as the seed-photon source, has been applied to fit the rms amplitude and phase lag spectra of type C QPOs in MAXI J1535–571, using *Insight*-HXMT data in the 1–100 keV energy range (Zhang et al. 2022).

The transient BHXRB H 1743–322 was first observed by *Ariel-V* satellite in 1977 August (Kaluzienski & Holt 1977), located at RA = $17^{\text{h}}46^{\text{m}}15^{\text{s}}.596$ and Dec = $-32^{\circ}14'00''.860$. Based on the X-ray/radio observations of the two-sided jet in the 2003 outburst, Steiner et al. (2012) determined a distance of 8.5 ± 0.8 kpc, and an inclination angle of $75^{\circ} \pm 3^{\circ}$, respectively. By applying the relativistic accretion disc model in the spectral fitting, they also estimated a black hole spin of $a_* = 0.2 \pm 0.3$. H 1743–322 is an active black hole transient source and was monitored by *RXTE* to undergo outbursts frequently between 2003 and 2011. The 2003 outburst is the brightest one with observations in multiple wavelengths (see Parmar et al. 2003; Homan et al. 2005; McClintock et al. 2009), then two much fainter outbursts in 2004 and 2005, respectively, followed behind (Bhattacharjee et al. 2017; Coriat et al. 2011). In 2008, two outbursts (2008a and 2008b) were observed in both of X-ray and radio bands, but the 2008a outburst is classified as failed-transition outburst for the short outburst cycle without experiencing soft states (Capitanio et al. 2009; Jonker et al. 2010; Coriat et al. 2011). Then this source entered into a new outburst during 2009 (Chen et al. 2010; Motta et al. 2010), and exhibited the last three outbursts in 2010 (2010a and 2010b) and 2011 (Zhou et al. 2013). Recently, Aneesha & Mandal (2020) systematically analysed the spectral evolution of the outbursts of H 1743–322 in the *RXTE* era. In the post *RXTE* era, there were 2012, 2014, 2016 and 2018 outburst monitored by other instruments (Shidatsu et al. 2014; Stiele & Yu 2016; Chand et al. 2020; Williams et al. 2020; Wang et al. 2022).

In this work, we systematically investigate type C QPO data born out of *RXTE* observations in both of the rise and decay phases of seven outbursts from H 1743–322. We introduce observations and data reductions in Section 2, present the data analysis and results in Section 3, discuss these in Section 4 and finally summarize in Section 5.

2. OBSERVATIONS AND DATA REDUCTIONS

Fig. 1 shows the *RXTE*/All Sky Monitor (ASM) light-curve of H 1743–322 in the 1.5–12 keV energy band. Between 2003 and 2011, this source experienced nine outbursts, and we focus on the 2003, 2008a, 2008b, 2009, 2010a, 2010b and 2011 outburst which contain abundant type C QPO observations carried out by *RXTE*. The *HEASOFT* software package version 6.28 is used for the data analysis. We generate good time intervals (GTIs) with the constraints that the elevation angle (ELV) is larger than 10° and angular distance between the pointing position and source (OFFSET) is less than 0.02° . The standard data products of e.g. light curve, spectrum and background are produced from observational data of Proportional Counter Array (PCA). Since combining large spectral data sets with different PCA configurations can produce large systematic errors (see Smith et al. 2009), we only use data from Proportional Counter Unit (PCU) 2 in our subsequent spectral analysis because it is the only unit which was 100% on during the observations. Data of standard 2 mode are adopted for the spectral analysis in the energy range of 3–30 keV without any groupings and binnings. To account for calibration uncertainties, a systematic error of 0.5 per cent is added to spectral fittings. We generate the power density spectrum (PDS) using the light curve born out of ‘Event’ and ‘Binned’ modes in the energy range of 3–30 keV (PCA channels 7–71 of the calibration epoch 5¹), which is the same as that of the spectral fittings. Then both of the spectral and timing analyses are performed using XSPEC version 12.12.0.

3. ANALYSIS AND RESULTS

3.1. Power Density Spectra

For each observation in the present study, we produce the PDS in the 1/64–64 Hz frequency range with the 8-ms time resolution by taking Miyamoto normalization (Belloni & Hasinger 1990; Miyamoto et al. 1991). All the PDS are fitted with several Lorentzian functions (see Fig. 2). In the PDS fittings, we use at least two Lorentzian functions to fit the broad band noise and QPO signal, respectively. The centroid frequency of the Lorentzian fitted the low-frequency broad band noise is fixed at zero. However, if there are any other significant residual structures (e.g. the second QPO harmonic), more Lorentzian functions would be added to the fitting model. Since we primarily focus on the QPO signal, whether to add more Lorentzians depends on whether the Lorentzian functions used to fit the QPO harmonics describe the QPO components well in the case of

¹ <https://heasarc.gsfc.nasa.gov/docs/xte/e-c-table.html>

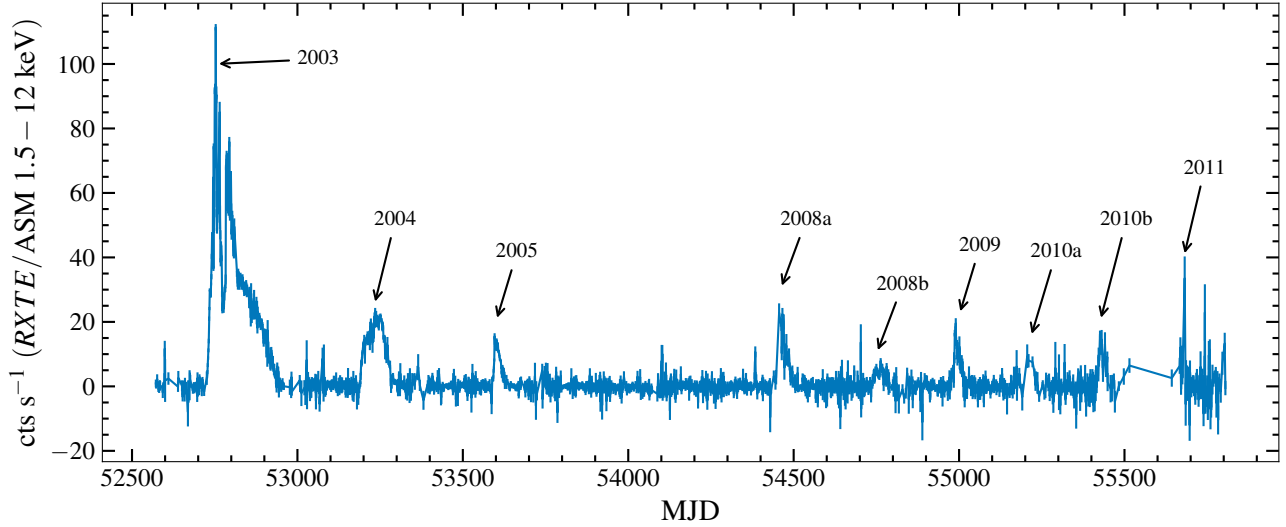


Figure 1. The *RXTE*/ASM light curve of H 1743–322 in the 1.5–12 keV energy band with a resolution of one point per day. In the *RXTE* era, there are nine outbursts between 2003 and 2011, where we focus on the 2003, 2008a, 2008b, 2009, 2010a, 2010b and 2011 outburst which contain abundant type C QPO observations.

the current total model. To do this, after fitting with the current model, we retain the best-fit parameters and remove the Lorentzian components fitted the QPO harmonics to check whether the residual structures from the data/model ratio plots are Lorentzian-like shapes and broad band noises are well fitted. Following Motta et al. (2015), if a QPO consists of multiple harmonic peaks, the QPO fractional rms is computed by adding in quadrature the rms of the harmonic peaks (i.e. QPO fractional rms is computed by $\sqrt{\sum P_i}$, where P_i is the power calculated with integration of the i -th QPO harmonic Lorentzian function). Additionally, considering the background contribution, the QPO fractional rms reported in the present study is finally computed by

$$\text{rms} = \sqrt{\sum_i P_i \times [(S + B)/S]}, \quad (1)$$

where S and B are the source and background average rate, respectively (see Bu et al. 2015). The best-fit QPO parameters of the present study are presented in Appendix D.

3.2. Energy Spectra

In our spectral fittings, the Galactic absorption effect is always included in our models by implementing *tbabs* model (Wilms et al. 2000). The hydrogen column density (N_H) is fixed to $2.3 \times 10^{22} \text{ cm}^{-2}$ following Miller et al. (2006). Firstly, we start with a simple model consists of a power-law and a disc blackbody component (Model 1: $tbabs \times (diskbb + powerlaw)$) and obtain large reduced- χ^2 ($\gg 2$) in the most observations. Then we replace *powerlaw* with *nthcomp*,

a physically motivated thermal Comptonization model which describes the spectrum of Compton upscattering photons (Zdziarski et al. 1996; Życki et al. 1999). The spectral fitting with the second model (Model 2: $tbabs \times (diskbb + nthcomp)$) gives a smaller reduced- χ^2 but, as shown in Fig. 3a and b, the residuals still show obvious structures at energies around the iron line ($\sim 6.4 \text{ keV}$) and Compton hump ($\sim 10\text{--}30 \text{ keV}$), providing evidence of a relativistic reflection component (García et al. 2013, and references therein). Hence we add a reflection model *relxillcp* (Dauser et al. 2014; García et al. 2014) in our spectral fittings (Model 3: $tbabs \times (diskbb + nthcomp + relxillcp)$).

For the spectral fitting with Model 3, we link the seed photon temperature (kT_{bb}) of *nthcomp* with the inner disk temperature (kT_{in}) of *diskbb* and choose the flavor of disk-blackbody seed photons for *nthcomp*. Since *relxillcp* calculates the reflection component using the *nthcomp* continuum, it is self-consistent to link the relevant parameters like the photon index (Γ) and electron temperature (kT_e) between two models. In the reflection model *relxillcp*, we assume the canonical power-law emissivity profile, $\epsilon \propto r^{-3}$, for the disc (Fabian et al. 1989). The parameter R_{out} is the outer radius of the accretion disc which turns out to be not sensitive to the overall fitting and hence is frozen at the maximum value ($1000R_g$, where $R_g = GM/c^2$ is the gravitational radius). In order to make *relxillcp* only calculate the reflection component, we fix the reflection fraction (R_f) to -1 . Referring to previous studies, the disc inclination (i), spin parameter of the black hole (a_*) and iron abundance (A_{Fe} , in solar units) are set to 75° , 0.2 and 3.0,

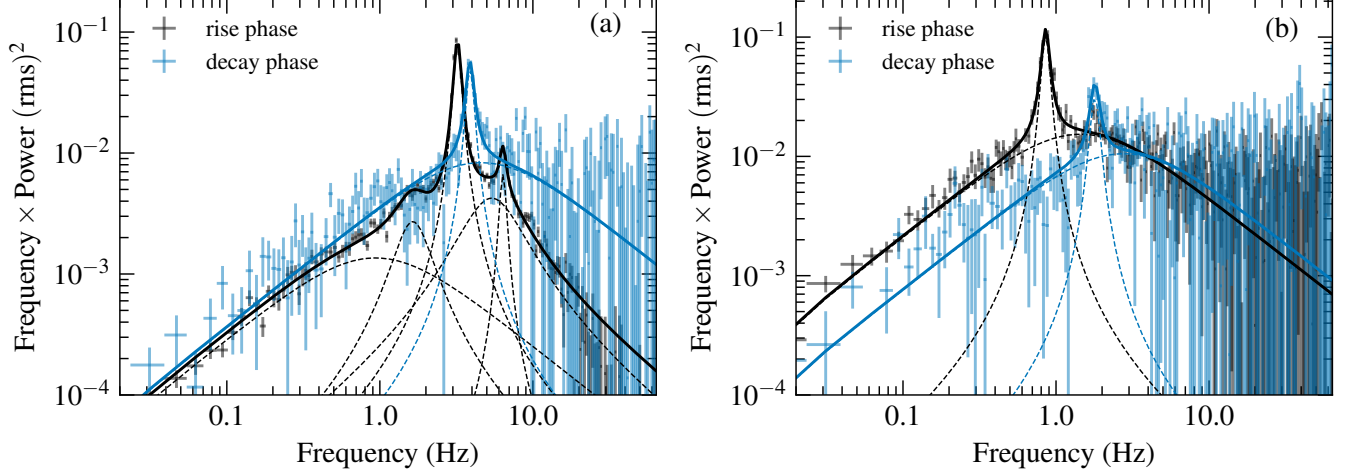


Figure 2. Representative power density spectra from the outburst rise (plotted in black) and decay phase (plotted in blue). Power density spectra are produced in the 3–30 keV energy range and 1/64–64 Hz frequency range, then fitted with the model consisting of multiple Lorentzian functions (dotted lines). For panel (a), strong QPO components appear at high frequencies ($f_{\text{QPO}} > 2$ Hz), where QPO amplitudes of the two outburst phases are comparable. For panel (b), the QPO components appear at low frequencies ($f_{\text{QPO}} < 2$ Hz), where QPO amplitude of the rise phase is significantly larger than that of the decay phase.

respectively (Steiner et al. 2012; Chand et al. 2020). The shape of *nthcomp* continuum is set by the combination of the electron temperature (kT_e) and scattering optical depth (τ_s), where the higher cut-off energy is parameterized by kT_e (Życki et al. 1999). However, in many observations, the cut-off energy is beyond the energy band of our spectral analysis (3–30 keV). Although kT_e can influence the reflection hump at energies around 20–40 keV which gives a chance to estimate it beyond the spectral coverage (see García et al. 2015a), we note that kT_e is not completely reliable in our spectral fitting. For a less constrained kT_e , we fix it to 300 keV. Additionally, we notice the *diskbb* contribution is marginal in where its parameters are not well constrained by using only PCA data and the spectral fitting does not even need this component in some observations (see also Plant et al. 2014; Aneesha et al. 2019). For these observations, we fix the parameter kT_{in} and normalization of *diskbb* at 0, then let kT_{bb} of *nthcomp* as a free parameter in the fitting. We calculate the unabsorbed flux for each component in the energy range 3–30 keV by convolving *cflux* model with these required models. After fitting energy spectra with Model 3, we obtain a reasonable reduced- χ^2 (~ 1) for most observations (see Appendix A) and compute the 90 per cent confident-level uncertainties using the Markov Chain Monte Carlo (MCMC) technique, with length 40 000. The best-fit parameters of the two representative spectra presented in Fig. 3 with Model 3 are summarized in Table 1.

3.3. Timing-spectral Joint Analysis

The timing and spectral analyses presented in Section 3.1 and 3.2, respectively, provide the essential in-

Table 1. Best-fit Parameters and the Corresponding 90% Confidence Intervals Obtained from Fitting the Representative *RXTE*/PCA Spectra Presented in Fig. 3 Using the Model 3: *tbabs* \times (*diskbb* + *nthcomp* + *relxillcp*).

Model	Parameters	Rise Phase	Decay Phase
<i>tbabs</i>	N_{H} (10^{22}cm^{-2})	2.3 (fixed)	
<i>relxillcp</i>	i (Deg)	75 (fixed)	
	a_*	0.2 (fixed)	
	R_{out} (R_{g})	1000 (fixed)	
	q^a	3 (fixed)	
	A_{Fe} (Solar Units)	3 (fixed)	
	R_{f}	−1 (fixed)	
<i>diskbb</i>	T_{in} (keV)	$0.76^{+0.05}_{-0.05}$	$0.62^{+0.08}_{-0.18}$
	N_{disk}^b	866^{+280}_{-201}	99^{+842}_{-53}
<i>nthcomp</i>	Γ	$2.29^{+0.04}_{-0.03}$	$1.83^{+0.03}_{-0.05}$
	kT_e (keV)	$8.6^{+1.0}_{-0.5}$	300(fixed)
	N_{nth}^c	$2.52^{+0.29}_{-0.21}$	$0.15^{+0.05}_{-0.08}$
<i>relxillcp</i>	R_{in} (R_{ISCO})	$17.9^{+76.8}_{-8.1}$	100 (fixed)
	$\log_{10}(\xi)^d$	$2.81^{+0.13}_{-0.17}$	$3.53^{+0.67}_{-0.31}$
	(erg cm s^{-1})		
	N_{rel}^e (10^{-3})	$42.0^{+17.1}_{-9.7}$	$2.3^{+4.50}_{-0.10}$
	$\chi^2/\text{d.o.f}$	50.18/46	38.29/48

NOTE—^a The power-law index of the emissivity profile ($\epsilon \propto r^{-q}$). ^b Normalization of *diskbb* model. ^c Normalization of *nthcomp* model. ^d Log of the ionization parameter (ξ) of the accretion disc, where $\xi = L/nR^2$, with L as the ionizing luminosity, n as the gas density, and R as the distance to the ionizing source. ^e Normalization of *relxillcp* model.

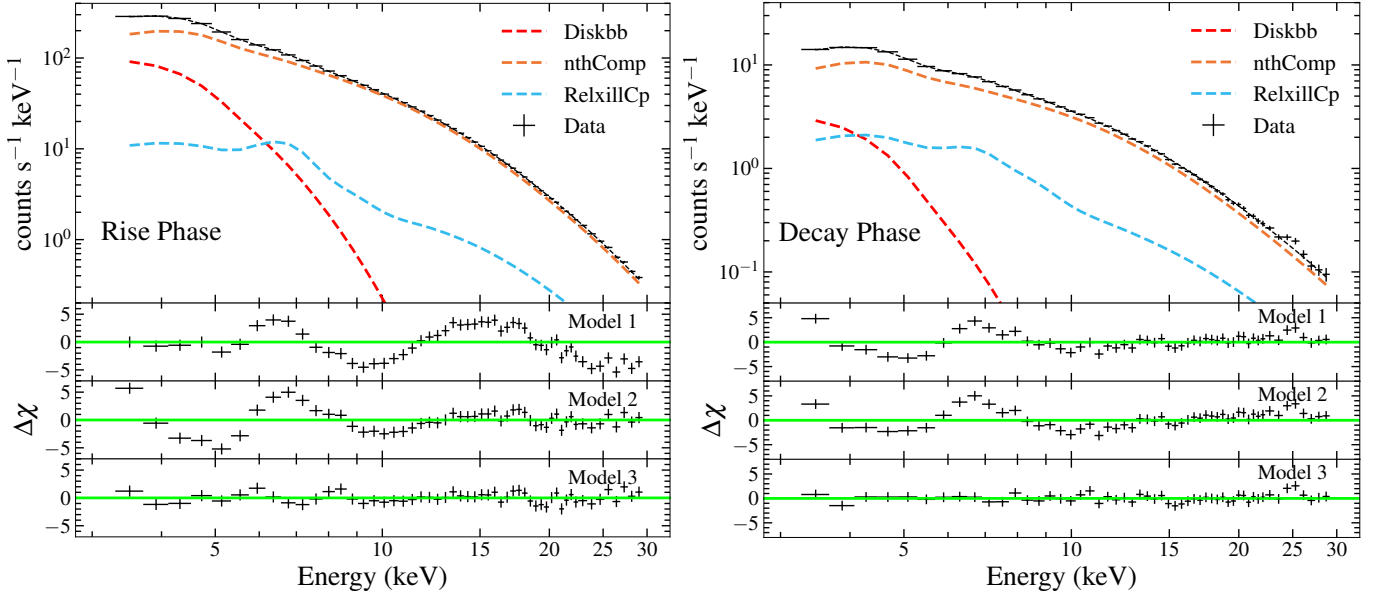


Figure 3. Representative *RXTE*/PCA energy spectra (the top panels) and fitting residuals (the three bottom narrow panels) are plotted for Model 1, 2 and 3, respectively) for both of the rise phase (the left panel, obs.ID: 80146-01-30-00) and the decay phase (the right panel, obs.ID: 93427-01-04-00). The *diskbb*, *nthcomp* and *relkillcp* model are plotted in red, orange and blue, respectively.

puts for a spectral-timing joint diagnostic of the outburst what is shown in follows.

3.3.1. Correlations between the QPO rms and non-thermal component

Fig. 4 presents the relations between the QPO fractional rms and non-thermal component during the rise and decay phases, separating the different outbursts. For clarity's sake, data points of the rise phase from different outbursts are displayed in different colors and shapes in Fig. 4a and b, and the data points of the decay phase are plotted in gray without separating different outbursts, while in the Fig. 4c and d, we display data sets in the opposite way. As shown in Fig. 4a, in the rise phase, there are no remarkable correlations between the fractional rms and non-thermal fluxes (F_{nthcomp}), and data points from different outbursts distribute widely in F_{nthcomp} which is consistent with the large differences in the outburst peak fluxes shown in Fig. 1. However, if we display the QPO fractional rms as a function of the non-thermal fraction ($F_{\text{nthcomp}}/F_{\text{total}}$), the positive correlations between the fractional rms and non-thermal component become significant and consistent among different outbursts (see Fig. 4b). In the decay phase, different outbursts show the similar non-thermal fluxes ($\sim 10^{-9}$ ergs cm⁻² s⁻¹). However, compared with the rise phase, the positive correlation between the fractional rms and non-thermal fraction is not clear within the decay phase because of the relatively larger error bar of the non-thermal fraction (see Fig. 4c and d).

3.3.2. QPO rms dependence on frequency

Type C QPOs usually appear in the HIMS, a stage shows the significant transition in both of the timing and spectral domains (Homan & Belloni 2005; Remillard & McClintock 2006), where properties of the type C QPO, like central frequency and fractional rms, evolve in a large value range. Previous studies have presented that the fractional rms of type C QPOs varies with the frequency (see Motta et al. 2015; van Doesburgh & van der Klis 2020; Zhang et al. 2020; Wang et al. 2022). Here, we analyse a number of type C QPO samples across different outbursts of H 1743-322 and present the QPO fractional rms dependence on fundamental frequency in both the rise and decay phases in Fig. 5a for comparisons. Data points displayed are not be distinguished among different outbursts, but only between the rise and decay phases. As one can see, during the rise phase, the QPO fractional rms increases slightly with frequency below 1 Hz and then remains roughly flat around 1–2 Hz, while shows a significant drop at higher frequencies. However, the presented relation of the decay phase deviates from that of the rise phase at low frequencies, where the deviation becomes larger for the lower frequency. Also, these relations between the QPO fractional rms and frequency in both of the rise and decay phases are consistent among different outbursts. The fractional rms presented in the study is computed by adding in quadrature the rms of the harmonic peaks. However, we have checked the case that taking the rms of QPO fundamen-

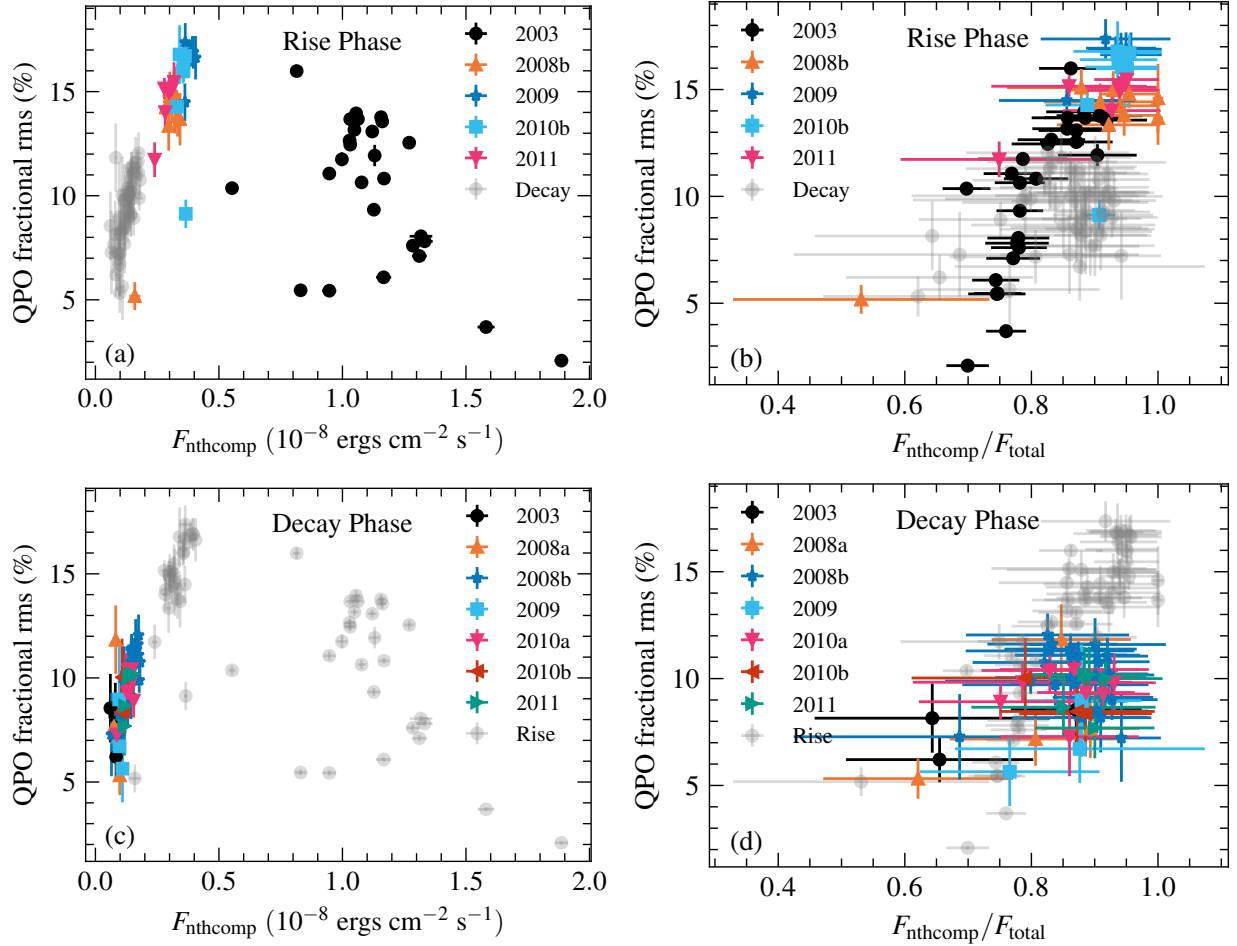


Figure 4. The relations between QPO fractional rms and the non-thermal component. For clarity's sake, data of the different outburst rise phases are displayed in different colors in the panels (a) and (b), and data points of the decay phases are plot in gray without separating different outbursts, while the panels (c) and (d) display the data points of the rise and decay phases in the opposite way.

tal only, and find the dependence of fractional rms on frequency deviates only slightly with respect to the results presented in Fig. 5, where the two outburst stages remain different branches in the relations between QPO fractional rms and frequency clearly.

Since the fractional rms is defined as the fractional variability of the flux, the fractional rms we compute in the Section 3.1 and presented in Fig. 5a can be described by

$$\text{rms} = \frac{F_{\text{var}}}{F_{\text{total}}} = \sigma \times \frac{F_c}{F_{\text{total}}}, \quad (2)$$

where F_{var} is the variable flux (absolute rms), F_{total} is the total time-averaged flux, σ is a function for the intrinsic rms, and F_c represents the flux contributing to the QPO variability (see also Kong et al. 2020; Shui et al. 2021). If we assume that only the non-thermal component contributes to the type C QPO, while the fractional rms is diluted by the other components, i.e. the thermal and reflected components, then F_c is equal

to F_{nthcomp} . So the intrinsic rms is the variability amplitude of non-thermal emission, which can be computed by

$$\sigma = \text{rms} \times \frac{F_{\text{total}}}{F_{\text{nthcomp}}}. \quad (3)$$

The dependence of the intrinsic rms on frequency is presented in Fig. 5b, and we find it is similar to that of the fractional rms displayed in Fig. 5a. It is clear to see the two separate branches of the rise and decay phases.

3.4. Coronal Parameters and Radio Emission

We have shown that the dependence of the QPO intrinsic rms (hereafter QPO rms) on frequency shows two branches: the QPO rms in the outburst rise phase is significantly larger than that in the decay phase at low frequencies. To investigate this bi-modality in more detail, we present the dependence of the rms- f_{QPO} relation on radio fluxes and spectral parameters in Fig. 6. The quasi-simultaneous measurements of the radio flux

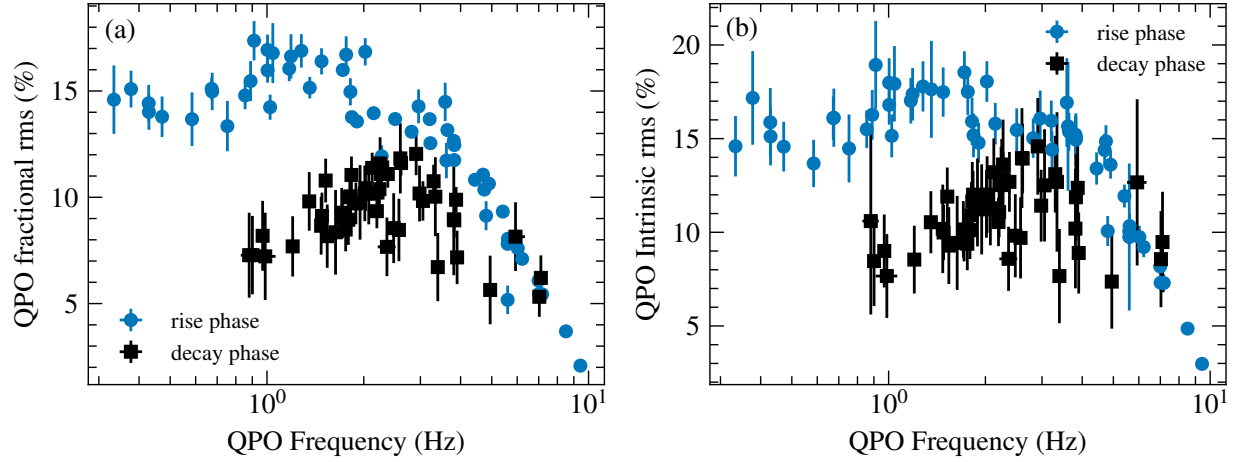


Figure 5. QPO fractional rms (the left panel) and intrinsic rms (the right panel) plotted as a function of frequency. The rise and decay phase are distinguished in different colors and shapes: data points from the rise phase are plotted as blue circles, while those from the decay phase are plotted as black squares.

density at ~ 8.5 GHz ($S_{\nu=8.5\text{GHz}}$) are taken from [McClintock et al. \(2009\)](#); [Jonker et al. \(2010\)](#); [Coriat et al. \(2011\)](#); [Miller-Jones et al. \(2012\)](#). For details of the radio observations used in the present study, see Appendix D. We note that not all *RXTE*/PCA observations in this study have quasi-simultaneous radio measurements. However, for clearly showing the radio dependence of the two different branches, we plot the entire QPO data set from our timing analysis in gray in the top two panels of Fig. 6, while coloring these data points which have radio observations. Furthermore, since 2003 outburst is much brighter than the other outbursts, we present the radio data of 2003 outburst in Fig. 6a alone, while those of the other outbursts are shown in Fig. 6b. The dependence of the coronal temperature (kT_e) and photon index (Γ) are presented in the bottom two panels of Fig. 6, respectively. The shade of the data points in each panel indicate the measured values of the parameters. Radio emission during the outburst rise phase of 2003 outburst is the strongest ($S_{\nu=8.5\text{GHz}} > 10$ mJy), while that of the other outbursts is relatively weaker ($S_{\nu=8.5\text{GHz}} \sim 2.5$ mJy). For an individual outburst, there is a marginally decreasing trend of the radio flux density from low QPO frequency ($f_{\text{QPO}} < 2$ Hz) to high frequency ($f_{\text{QPO}} \sim 8$ Hz). Additionally, radio emission of the decay phase ($S_{\nu=8.5\text{GHz}} < 1$ mJy) is significantly weaker than that of the rise branch. In contrast to the radio flux, the electron temperature is higher in the decay branch. These triangles plotted in Fig. 6c indicate that kT_e are too high to be constrained using *RXTE*/PCA energy spectra, hence fixed at 300 keV (see Section 3.2 for details). However, for the photon index, there are no apparent differences between the two branches in the similar frequency range.

3.5. Phenomenological Analysis with the L-T Precession Model

The phenomenon that the QPO rms is dependent on the frequency and outburst stage (see Fig. 5) indicates that the intrinsic properties of QPOs changed during the outburst. If type C QPOs are produced by the L-T precession of the entire corona (see [Ingram et al. 2009](#); [You et al. 2018](#)), a simplified geometrical model presented as follows can be used to estimate the intrinsic rms semi-quantitatively.

Using the coordinate system described by [Veledina et al. \(2013\)](#); [Ingram et al. \(2015\)](#), the unit vector pointing from the central black hole to the observer is given by

$$\hat{\mathbf{o}} = (\sin i \cos \Phi, \sin i \sin \Phi, \cos i), \quad (4)$$

where i is the binary inclination and Φ is the azimuth of the observer. The instantaneous normal of the corona is $\hat{\mathbf{n}}$, changing with the precession phase angle ω :

$$\hat{\mathbf{n}} = (\sin \beta \cos \beta (1 + \cos \omega), \sin \beta \sin \omega, \cos^2 \beta - \sin^2 \beta \cos \omega), \quad (5)$$

where β is the angle between binary orbit and black hole spin. We note that ω changes from 0 to 2π on the precession period, hence leads to the changes of $\hat{\mathbf{n}}$. Then cosine of the included angle (θ) between $\hat{\mathbf{n}}$ and $\hat{\mathbf{o}}$ can be written by

$$\begin{aligned} \cos \theta &= \hat{\mathbf{n}} \cdot \hat{\mathbf{o}} \\ &= \sin \beta \cos \beta \sin i \cos \Phi (1 + \cos \omega) \\ &\quad + \sin \beta \sin \omega \sin i \sin \Phi \\ &\quad + \cos i (\cos^2 \beta - \sin^2 \beta \cos \omega). \end{aligned} \quad (6)$$

We consider a simplified problem with assuming that the coronal shape is a crushed sphere, i.e. viewed from

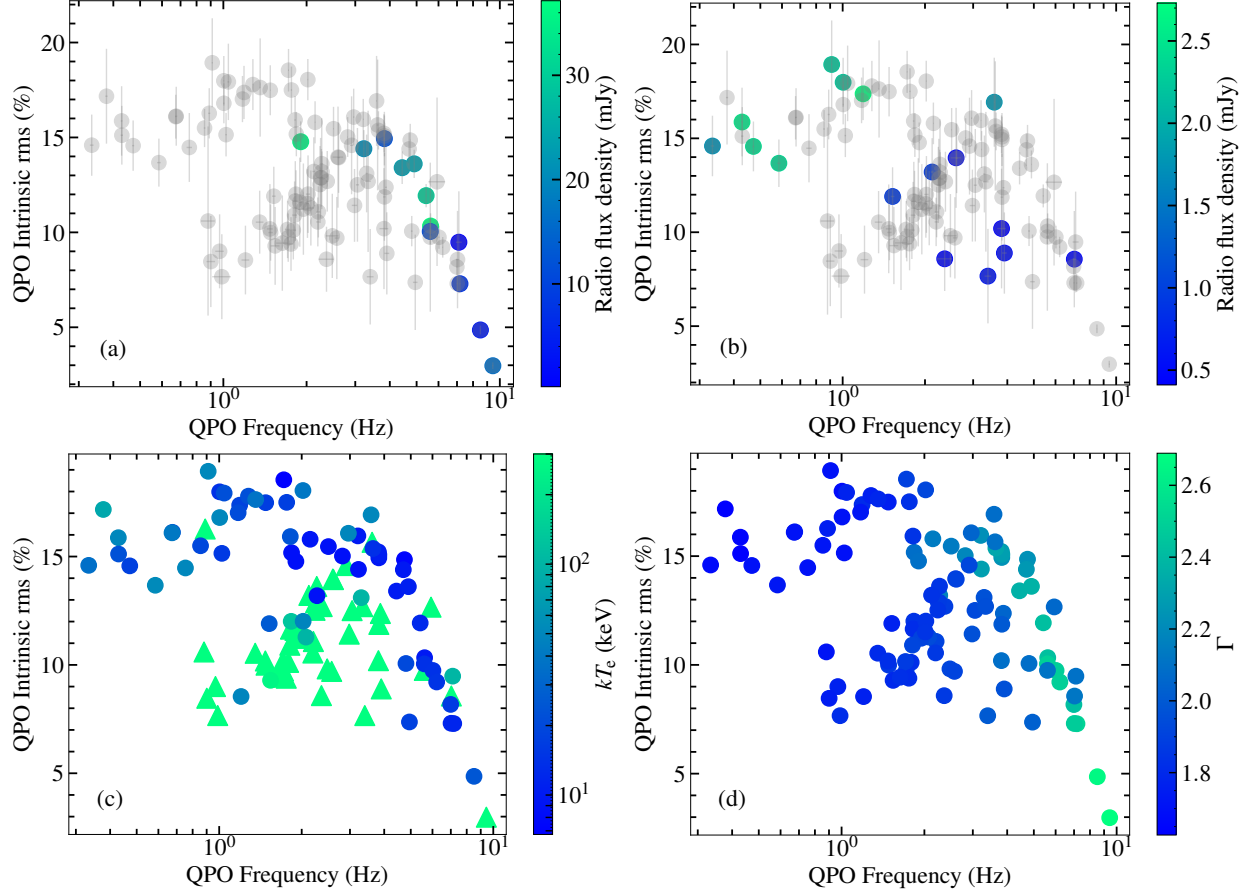


Figure 6. The QPO intrinsic rms plotted as a function of frequency. The shade of the data points indicate the quasi-simultaneous measurements of the radio flux density (a and b), kT_e (c) and Γ (d), respectively. In panels (a) and (b), we plot the entire QPO data set from our timing analysis in gray, only these data points with radio observations are colored. Furthermore, since the outburst 2003 is much brighter than the other outbursts, we present the radio flux density of the 2003 outburst in panel (a) alone, while those of the other outbursts are shown in panel (b). In panel (c), these triangles indicate that kT_e is too high to be constrained using *RXTE*/PCA energy spectra, hence fixed at 300 keV.

the coronal normal (\hat{n}) is a circle while the cross-section is an ellipse (see Fig. 7). The shape of the corona can be described by defining the scale height, h/r , where h is the semiminor axis and r is the semimajor axis of the ellipse, respectively. In the geometry described above, the projected area of the corona to the observer is

$$\begin{aligned} S_{\text{ob}} &= \pi r^2 \left[\sin^2 \theta \cdot (h/r)^2 + \cos^2 \theta \right]^{1/2} \\ &= \pi r^2 \left\{ (h/r)^2 + [1 - (h/r)^2] \cos^2 \theta \right\}^{1/2}. \end{aligned} \quad (7)$$

For simplicity, we assume the radiation of the corona is homogeneous and isotropic, then the observed flux from the corona is a function of θ and h/r :

$$\begin{aligned} F &= \bar{I} \cdot \Delta\Omega = \bar{I} \cdot S_{\text{ob}}/D^2 \\ &\propto \left\{ (h/r)^2 + [1 - (h/r)^2] \cos^2 \theta \right\}^{1/2} (1 - e^{-\tau}), \end{aligned} \quad (8)$$

where \bar{I} is the average radiation intensity, $\Delta\Omega$ is the solid angle of the corona in the view of the observer, D

is the distance from the source to the observer, and τ is the effective optical depth, also a function of θ and h/r . We estimate τ as a simple case:

$$\tau = \tau_0 \left\{ (h/r)^2 + [1 - (h/r)^2] \cos^2 \theta \right\}^{-1/2}, \quad (9)$$

where τ_0 is the minimum optical depth of the corona, i.e. viewed from the coronal normal (see Appendix B for details). Combining Equations 8 and 9, we find that the flux from the corona changes with θ on the precession period. On the basis of the above, the minimum and maximum coronal flux could be calculated in the ω value range $0 - 2\pi$. Then the QPO rms can be estimated by

$$\text{rms} = \frac{F_{\text{max}} - F_{\text{min}}}{F_{\text{max}} + F_{\text{min}}}, \quad (10)$$

where F_{max} and F_{min} are the maximum and minimum value of the coronal flux, respectively, on the precession period.

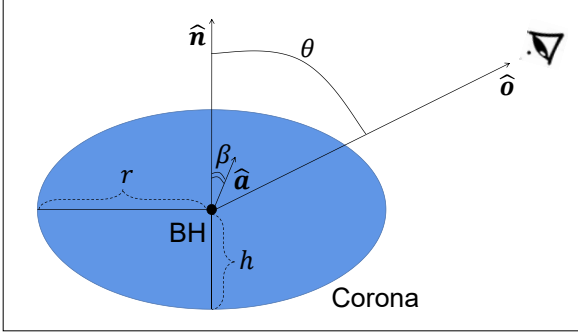


Figure 7. Schematic diagram illustrating the cross-section of the corona. \hat{n} , \hat{o} and \hat{a} represent the normal of the corona, unit vector pointing from the black hole to the observer and unit vector of black hole spin, respectively. β is the angle between binary orbit and black hole spin, and θ is the included angle between \hat{n} and \hat{o} . The coronal shape is described by the height scale h/r , the ratio of the semiminor and semimajor axis of the ellipse. We note this presented representative geometry is a case of $\Phi = 0$.

The calculated results using the simplified geometrical model are presented in Fig. 8. In our calculation, we assume a translucent corona with $\tau_0 = 1$ which is consistent with the previous hypotheses and simulations (see Ingram et al. 2015; You et al. 2018, 2020). Fig. 8a displays the intrinsic rms dependence on the entire range of viewing angles ($h/r = 0.2$), where it shows that rms increases with the inclination (i), while gets the peak values at $\Phi = 180^\circ$. However, i and Φ are constant for a specific black hole source, so the scale height (h/r) is the only parameter to influence intrinsic rms during the outburst evolution. In Fig. 8b, we find that QPO rms is highly dependent on h/r , especially in the high inclination sources ($i \sim 60^\circ - 90^\circ$). We note that the general relativity effects, e.g. light bending, are not considered in the simplified L-T precession model, but the results presented in Fig. 8 are consistent with previous studies which took the general relativity into account (see Veledina et al. 2013; Ingram et al. 2015; You et al. 2018). This fact indicates that GR effects, e.g. light bending, could be the second-order effects to affect the QPO rms in the L-T precession model.

Calculating with different values of h/r can obtain different intrinsic rms, which allows us to fit the relations between QPO intrinsic rms and frequency presented in Fig. 5b with the model. From a phenomenological motivation, we assume h/r as a quadratic function of f_{QPO} :

$$h/r = k_1 \cdot f_{\text{QPO}}^2 + k_2 \cdot f_{\text{QPO}} + k_3, \quad (11)$$

for both of the rise and decay phases, where f_{QPO} is the QPO frequency, k_1 , k_2 and k_3 are the model param-

eters. In this fitting, we fix the inclination, i , to 75° which is consistent with our spectral analysis and the misalignment angle, β , to 10° following Veledina et al. (2013) and Ingram et al. (2015). Since the azimuth of observer, Φ , is constant for a specific BH source, it only affects our estimation for the value of h/r , not the evolution trend, we fix it to a median (90°). The MCMC technique is used to carry out the parameter estimation with the uniform prior distribution. The posterior probability distributions of the model parameters are presented in Appendix C. From the fitting, we get $k_1 = (5.4 \pm 0.3) \times 10^{-3}$, $k_2 = (-1.96 \pm 0.27) \times 10^{-2}$, $k_3 = (3.39 \pm 0.05) \times 10^{-1}$ and $\chi^2/\text{d.o.f} = 65.90/53$ for the rise phase, while $k_1 = (7.5 \pm 2.9) \times 10^{-3}$, $k_2 = (-5.0 \pm 1.9) \times 10^{-2}$, $k_3 = (4.70 \pm 0.27) \times 10^{-1}$ and $\chi^2/\text{d.o.f} = 28.02/47$ for the decay phase. The fitting results are displayed in Fig. 9, where the trend lines and colored shaded regions represent the median and 3σ confidence intervals of the fitting, and the data points shown in the left panel are the same as those presented in Fig. 5b. In Fig. 9b, we display the h/r dependence on f_{QPO} (described by Eq. 11). The evolution trends of h/r are consistent between the two phases at high frequencies ($f_{\text{QPO}} > 4$ Hz), which show the increase with the increasing frequency. At low frequencies, h/r of both the two phases are negatively correlated to the frequency, but h/r values and the gradient of the decay phase are significantly larger than those of the rise phase.

4. DISCUSSION

We have systematically investigated the properties of type C QPOs by analysing one hundred and six *RXTE*/PCA observations across multiple outbursts of H 1743-322 from 2003 to 2011. Fig. 4 shows large variances of non-thermal fluxes among different outbursts, which distort the correlation between the non-thermal flux and the QPO fractional rms. However, the QPO fractional rms of different outbursts is positively correlated to the non-thermal fraction ($F_{\text{nthcomp}}/F_{\text{total}}$) consistently. Additionally, the co-evolution between the QPO intrinsic rms and frequency keeps similar traces among different outbursts (see Fig. 5). Since different outbursts could have very different luminosity levels, these consistent behaviours across outbursts indicate that the QPO intrinsic rms (hereafter QPO rms) is independent on the individual outburst brightness. However, the dependence of the QPO rms on frequency can be classified into two branches, where QPO rms in the outburst rise phase is significantly higher than that in the decay phase at low frequencies. Radio observations

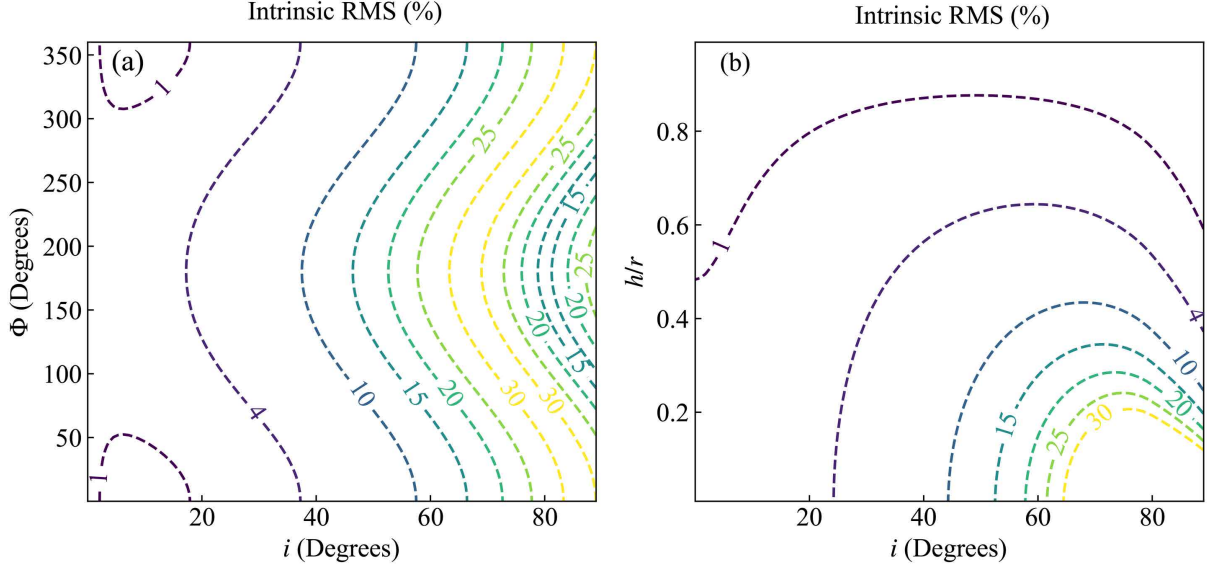


Figure 8. The calculated results using the geometrical model. In the calculation, we assume a translucent corona with $\tau_0 = 1$ which is consistent with the previous hypotheses and simulations (see You et al. 2018; Ingram & Motta 2019; You et al. 2020). Panel (a) displays the intrinsic rms dependence on the entire range of viewing angles with a fixed h/r value (0.2), panel (b) displays the dependence of intrinsic rms on h/r with different inclinations (Φ is set to 90°).

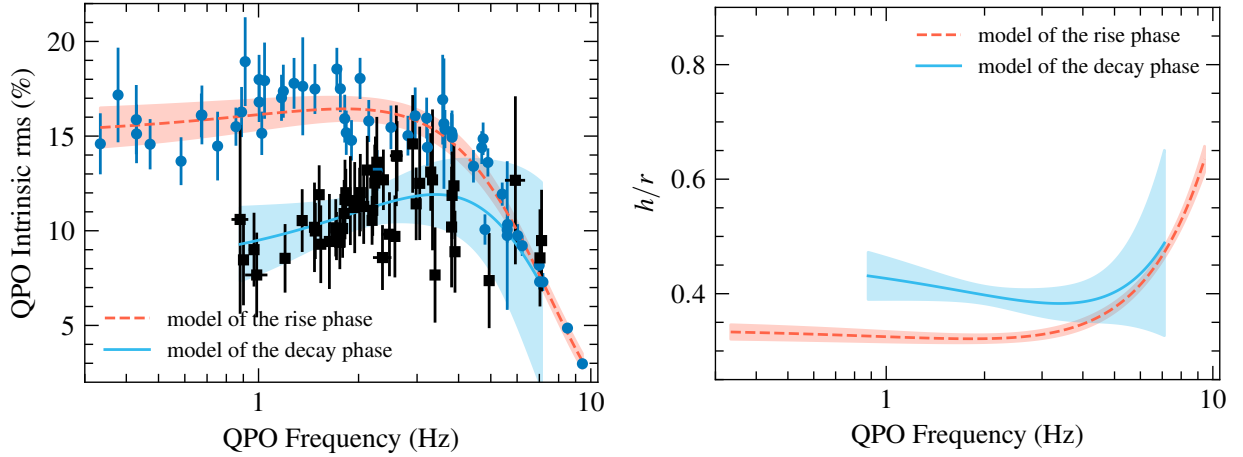


Figure 9. Fitting results of the relations between QPO intrinsic rms and frequency that presented in Fig. 5b with the simplified L-T precession model, where the trend lines and colored shaded regions represent the median and 3σ confidence intervals of the fittings: the rise phase is displayed in red and decay phase is display in blue. The data points plotted in the left panel are same as that presented in Fig. 5b.

and X-ray spectral analyses reveal more differences between the two branches.

4.1. Trace the Coronal Geometry with the Simplified L-T Precession Model

This phenomenon that the QPO rms is independent on the outburst brightness has been also reported in other sources (e.g. GX 339–4, Shui et al. 2021). If type C QPOs are produced by L-T precession of the corona, the X-ray QPO variability owes to the geometric wobble of the corona, which changes the projection area of the corona with respect to the observer to modulate the

X-ray flux (Ingram et al. 2009, 2015; You et al. 2018, 2020). Calculations presented in Section 3.5 give that the intrinsic amplitude is highly dependent on the coronal shape, h/r , for a specific BH source (assuming a translucent corona, $\tau \sim 1$). Accordingly, the similar QPO rms amplitudes with different outburst intensities indicate the coronal shape may not depend on the individual outburst brightness.

The left panel of Fig. 9 shows that, in the rise phase, the QPO rms increases slightly at low frequencies, while decreases sharply after reaching the peak value at ~ 2

Hz. In the dynamic part of the L-T precession model, f_{QPO} is negatively correlated to the outer radius, r , of the corona (Ingram et al. 2009), so the increasing f_{QPO} indicates a decreasing r . A possible explanation for the dependence of the QPO rms on frequency is that when the coronal outer radius (r) evolves, the coronal shape, i.e. h/r , changes synchronously. The fitting results of the rms- f_{QPO} relation with the simplified L-T precession model show that h/r of the rise and decay phases are consistent at high frequencies ($f_{\text{QPO}} > 3$ Hz), while h/r of the decay phase is larger than that of the rise phase in the low frequency range (see Fig. 9). The spectral analysis shows that the coronal temperature (kT_e) of the decay phase is obviously higher than that of the rise phase (see Fig. 6c). If the corona is a hot accretion flow (e.g. Advection-Dominated Accretion Flow, ADAF), it is mainly supported by the gas pressure (Narayan & Yi 1994; Yuan & Narayan 2014; Liu & Qiao 2022), and the height (h) could hence be larger with the higher coronal temperature. Accordingly, the corona in the decay phase could have relatively larger h/r at a specific frequency, and then precesses with a lower variability amplitude. This is because the variability of the coronal projection area with respect to the observer is smaller with a higher h/r value (see Fig. 8).

4.2. Qualitative Interpretation with the Time-dependent Comptonization Model

Time-dependent Comptonization models can explain quantitatively the rms spectrum and the phase lag spectrum of QPOs, by requiring coupled oscillations of the physical quantities: coronal temperature, kT_e , temperature of the source of seed photons, kT_s and the external heating rate, \dot{H}_{ext} (see Karpouzas et al. 2020; Bellavita et al. 2022). Although the QPO dynamic origin is not specified in these models, the recent proposal of Masticchiadis et al. (2022) that the QPO frequency arises from a resonance between the hot Comptonizing corona and the colder accretion disc via the coupling of the energy gains and losses in the system, could provide the dynamic part to the time-dependent Comptonization models, since the disc-corona coupling is also the mechanism suggested by these models to explain the QPO radiative properties. In the time-dependent Comptonization models, the fractional variability amplitude of QPOs (QPO fractional rms) is normalized by the variability amplitude of the external heating rate, $\delta\dot{H}_{\text{ext}}$, which is a fitting parameter. The energy-averaged rms in a specific energy range is therefore dependent on both the shape and the normalization ($\delta\dot{H}_{\text{ext}}$) of the rms spectrum. Karpouzas et al. (2021) and García et al. (2022) fitted the rms spectra and phase lag spectra of type C

QPO observations of GRS 1915+105 and found $\delta\dot{H}_{\text{ext}}$ is dependent on QPO frequency, where $\delta\dot{H}_{\text{ext}}$ is positively correlated strongly to f_{QPO} at low frequencies ($f_{\text{QPO}} < 1$ Hz), and negatively correlated to f_{QPO} in the narrow frequency range of 1–1.8 Hz, then decreases slightly from $f_{\text{QPO}} \sim 2$ Hz to $f_{\text{QPO}} \sim 6$ Hz. Since the rms dependence on f_{QPO} of H 1743–322 in the rise phase is similar to that of GRS 1915+105, the $\delta\dot{H}_{\text{ext}}$ dependence on f_{QPO} could also affect the rms- f_{QPO} relation of H 1743–322 in the rise phase. It may also work in the decay phase of H1743–322 if one considers in decay phase the positive and negative correlations at lower and higher frequencies, respectively. In Fig. 6, we show that the coronal temperature of the decay phase is higher than that of the rise phase, while there are no significant differences in photon index (Γ). In this case, as shown in Fig. 3 of Bellavita et al. (2022), the energy-averaged QPO rms in the energy range of 3–30 keV could be relatively lower in the decay phase. We propose the possible reason is that for the escaping photons in the specific energy range (3–30 keV), the higher coronal temperature indicates the less scatterings of the photons before escaping the Comptonizing medium, hence the effect of the variability amplitude amplification is weaker, if a balance between Compton cooling and external heating is at work for QPO amplification within the corona. We note that the above proposal is only qualitative, while the detailed investigation of the radiative properties of QPOs requires fitting the rms, phase lag, and time-averaged spectra simultaneously with the time-dependent Comptonization model (see Karpouzas et al. 2021; Méndez et al. 2022; García et al. 2022; Zhang et al. 2022).

4.3. Possible Relations Between Rms Differences and Hysteresis Effect

The most recent failed-transition outburst of H 1743–322, monitored by *Insight*-HXMT in 2018, has been reported by Wang et al. (2022). Different from the outbursts presented above, this outburst remained in the LHS and never showed the significant hysteresis trace in the HID throughout the observed stage (see Fig. 10a). The *Insight*-HXMT data of the 2018 outburst are taken from Wang et al. (2022). We plot the fractional rms dependence on f_{QPO} using both *Insight*-HXMT/ME and *RXTE*/PCA data in Fig. 10b. As one can see, in the 2018 outburst, the QPO fractional rms remains roughly constant with a value $\sim 12\%$ without significant differences between the rise and decay phases. The 2008b outburst is also classified into failed-transition outbursts, however, the system experienced the LHS-HIMS transition and a hysteresis trace in the HID during this out-

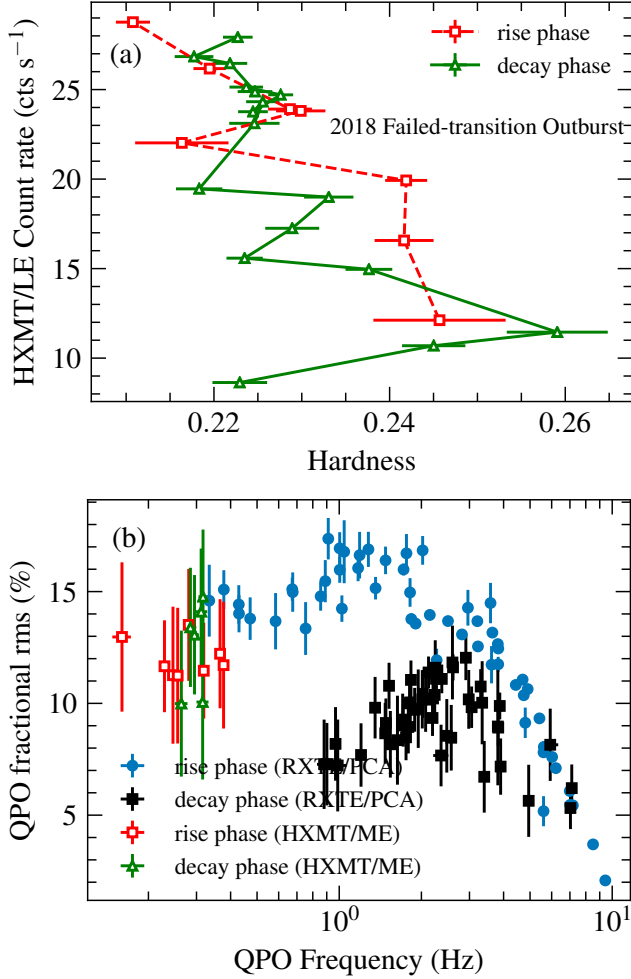


Figure 10. The hardness-intensity diagram (HID) of the 2018 failed-transition outburst monitored by HXMT/LE (the top panel) and correlation between QPO rms and frequency using data from both of *RXTE*/PCA and HXMT/ME (the bottom panel). The data of *Insight*-HXMT are taken from Wang et al. (2022). The top panel displays the HID with separating the rise and decay phases: the rise data are plotted as red hollow squares, while the decay data are plotted as green hollow triangles. The bottom panel displays the correlations with separating data sets from different instruments and outburst phases.

burst (see Coriat et al. 2011), with the rms differences between rise and decay phases which are consistent with those of other complete outbursts (see Fig. 5). On the basis of the above, the different rms- f_{QPO} relations between the rise and decay phases seem to be associated with the hysteresis trace in the HID, because these two phenomena accompany each other in H 1743–322. However, details about the relations between the rms differences and hysteresis effect need further investigations using more observational samples from more sources.

4.4. Possible Scenario of the Corona-jet Coupling in H 1743–322

Radio emission of BHXRBs is thought to be strongly related to relativistic jets (Fender 2001), which can also produce the Comptonization of soft photons from the disc (see Band & Grindlay 1986; Georganopoulos et al. 2002; Reig & Kylafis 2021). The jet is believed to be coupled to the accretion flow, but the nature of this connection is still not well understood. Based on a large dataset of *RXTE* observations, frequent radio observations and the time-dependent Comptonization model, a series of studies have revealed a possible picture of the corona-jet coupling in GRS 1915+105 (see Zhang et al. 2020; Karpouzas et al. 2021; Méndez et al. 2022; García et al. 2022). In H 1743–322, although quasi-simultaneous radio observations are not as abundant as that in GRS 1915+105, for each individual outburst, there is a marginally decreasing trend of the radio flux density from low QPO frequency (< 2 Hz) to high QPO frequency (~ 8 Hz) in the rise phase (see Fig. 6), which indicates a quenching compact jet during the hard-to-soft state transition. van den Eijnden et al. (2017) found that the QPO hard phase lag became negative at high frequencies. Following the idea of the time-dependent Comptonization model (see Karpouzas et al. 2020; Bellavita et al. 2022), the nature of the hard lag (positive lag) is Comptonization, in which hard photons could experience more scatterings than soft ones before escaping the medium. The phase lag becomes negative due to the *feedback* mechanism: the hard Comptonized photons may return back to the disc and be re-emitted later, so the softer photons could arrive later (Lee & Miller 1998). Based on the above, we propose that the scenario of the corona-jet coupling in GRS 1915+105 can be applied to the rise phase of H 1743–322. At low QPO frequencies where the radio emission is strong, the Comptonizing medium is dominated by the jet-like corona, where the phase lag is positive (see van den Eijnden et al. 2017). However, at high QPO frequencies where the radio emission is weak, the jet is quenched and replaced by an extended corona, which covers the inner parts of the thin disc. Since the disc has a large solid angle to receive the returning back photons, the *feedback* effect could be strong enough to produce the observed negative phase lag (van den Eijnden et al. 2017). We refer readers to Méndez et al. (2022) for details about the physical picture of the coupling between the corona and the jet. In the outburst decay phase, the coronal temperature is relatively higher and the radio emission is weaker. If the corona is powered by the magnetic energy (Merloni & Fabian 2001), especially as the case that the jet and the coronal power are tapped

from the common magnetic energy reservoir (see Malzac et al. 2004), the higher coronal temperature in the decay phase could be associated with the relatively weaker radio emission. On the basis of the above, we propose for H 1743–322 a similar scenario as the one proposed for GRS 1915+105 (Méndez et al. 2022) which, as in that case, would account for the differences of the radio emission and coronal temperature between the two outburst stages. During the outburst decay phase, the magnetic field lines are disorganized and the magnetic energy is mainly dissipated stochastically in the corona, probably via magnetic reconnection, hence the jet is quenched and the coronal temperature is high. However, the magnetic configuration could be very different during the earlier stage of the rise phase ($f_{\text{QPO}} < 2$ Hz and the phase lag is positive), where the magnetic field lines are spatially coherent with a large scale poloidal component, which could channel materials out of the corona and collimate them in the direction perpendicular to the disc, then the Comptonization mainly occurs in the jet. During the hard-to-soft transition, the magnetic field lines vary from the coherent to the disorganized configuration, the jet is quenched and replaced by the extended corona. Such a different journey experienced by the accretion flow in the rise and decay phases may play a role in the difference seen in the rms-frequency relation (see Fig. 5).

5. CONCLUSIONS

We performed systematic analyses of type C QPO observations from seven outbursts of H 1743–322 caught in the *RXTE* era. With a number of observational samples, we confirm the independence of the type C QPO intrinsic rms on the individual outburst brightness

which has been reported as well in GX 339–4. However, the dependence of QPO rms on frequency shows two branches in the outburst rise and decay phases, where the radio flux and coronal temperature are also different between the two phases. Both of the L-T precession model and the time-dependent Comptonization model can account for the rms difference, where the former needs a variable coronal geometric shape. Combining the recent *Insight*-HXMT observations of this source during its failed-transition outburst, we suggest such the rms difference between the two outburst stages could be also related to the hysteresis effect in the HID. The co-evolution among the radio flux, coronal temperature and phase lags indicates there could be corona-jet transitions in H 1743–322 which have been recently reported in GRS 1915+105.

1 We are grateful to the anonymous referee for con-
 2 structive comments that helped us improve this pa-
 3 per. This research has made use of data obtained
 4 from the High Energy Astrophysics Science Archive Re-
 5 search Center (HEASARC), provided by NASA’s God-
 6 dard Space Flight Center, and the *Insight*-HXMT mis-
 7 sion, a project funded by China National Space Ad-
 8 ministration (CNSA) and the Chinese Academy of Sci-
 9 ences (CAS). This work is supported by the National
 10 Key R&D Program of China (2021YFA0718500) and
 11 the National Natural Science Foundation of China un-
 12 der grants, U1838201, U1838202, 12173103, U2038101
 13 and U1938103. This work is partially supported by In-
 14 ternational Partnership Program of Chinese Academy of
 15 Sciences (Grant No.113111KYSB20190020).

APPENDIX

A. THE DISTRIBUTION OF REDUCED CHI-SQUARE IN THE SPECTRAL FITTING

In this section, we show the reduced chi-square (χ_{red}^2) distribution of the spectral fitting with the Model 3 presented in Section 3.2 (see Fig. 11). There are one hundred and six observational samples in our spectral analysis.

B. CALCULATION DETAILS OF THE CORONAL OPTICAL DEPTH

We consider a simplified coronal geometry with assuming the coronal shape is a crushed sphere (see Section 3.5). As a simplified model, the general relativity effects and Comptonization processes are neglected in our calculations. The effective optical depth of the corona is

$$\tau = \alpha L, \quad (\text{B1})$$

where α is the absorption coefficient, L is the average size of the corona in the view of the observer. We can define the three-dimensional Cartesian coordinates xyz , where the z -axis is consistent with the normal of the corona (\hat{n}), and the unit vector of the observer, \hat{o} , is in the yz plane. Then the ellipsoidal equation of the coronal surface is written by

$$\frac{x^2 + y^2}{r^2} + \frac{z^2}{h^2} = 1, \quad (\text{B2})$$

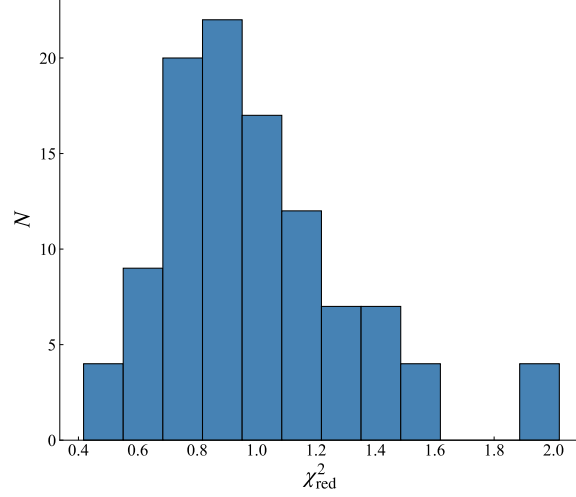


Figure 11. The reduced chi-square (χ^2_{red}) distribution of the spectral fitting with the Model 3 presented in Section 3.2.

where r is the coronal radius and h is the coronal height. We consider that the distance between the source and observer is far larger than the coronal radius (i.e. $D \gg r$), so the photon trajectories from the corona to the observer can be described as a cluster of parallel lines which are perpendicular to the x -axis. Then the linear equation of a representative photon trajectory to the observer is

$$\begin{aligned} z &= \cot \theta \cdot y + z_0 \\ x &= x_0, \end{aligned} \quad (\text{B3})$$

where θ is the include angle between \hat{n} and \hat{o} , z_0 is the z -intercept of the projection of the line in the yz plane, and x_0 is the x -intercept of the projection of the line in the xy plane, respectively. Then the length of the corona which contributes to the flux in the direction of the representative photon trajectory is

$$l = \sqrt{1 + \cot^2 \theta} \frac{2hr \sqrt{\left(1 - \frac{x_0^2}{r^2}\right) h^2 + \left(1 - \frac{x_0^2}{r^2}\right) r^2 \cot^2 \theta - z_0^2}}{h^2 + r^2 \cot^2 \theta}, \quad (\text{B4})$$

i.e. the length of the line cut by the ellipsoidal surface. The average size of the corona in the view of the observer can be calculated by

$$\begin{aligned} L &= \frac{\int_{-r}^r \int_{-s}^s l(x_0, z_0) dz_0 dx_0}{\int_{-r}^r \int_{-s}^s dz_0 dx_0} \\ &= \frac{4}{3} h \left\{ (h/r)^2 + \left[1 - (h/r)^2\right] \cos^2 \theta \right\}^{-1/2}, \end{aligned} \quad (\text{B5})$$

where $s \equiv \sqrt{[1 - (x_0/r)^2] h^2 + [1 - (x_0/r)^2] r^2 \cot^2 \theta}$. When $z_0 = \pm s$, the line of Eq. B3 is tangent to the ellipsoidal surface. Based on Eq. B1 and B5, the optical depth can be written by

$$\tau = \frac{4}{3} \alpha h \left\{ (h/r)^2 + \left[1 - (h/r)^2\right] \cos^2 \theta \right\}^{-1/2}. \quad (\text{B6})$$

We define $\tau_0 \equiv \frac{4}{3} \alpha h$, where τ_0 is the minimum optical depth of the corona, i.e. viewed from the coronal normal ($\theta = 0$), then the optical depth can be written by

$$\tau = \tau_0 \left\{ (h/r)^2 + \left[1 - (h/r)^2\right] \cos^2 \theta \right\}^{-1/2}. \quad (\text{B7})$$

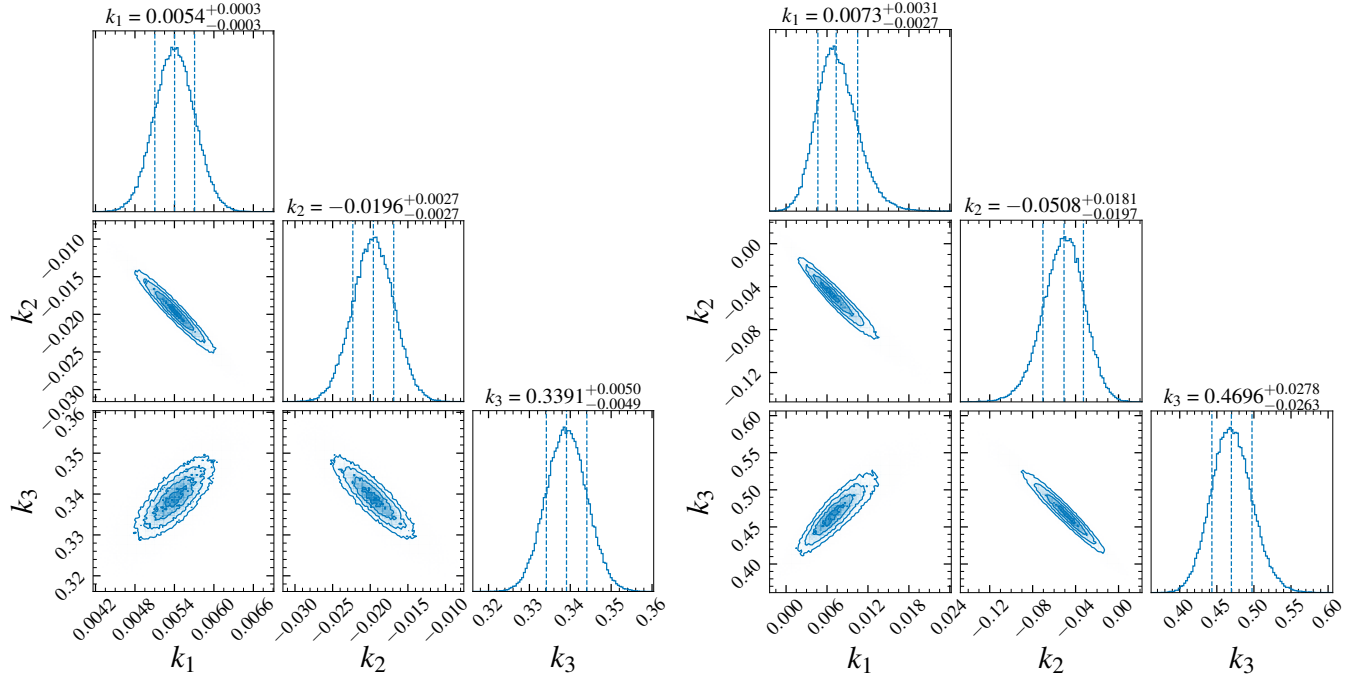


Figure 12. One- and two-dimensional projections of the posterior probability distributions, and the 0.16, 0.5 and 0.84 quantile contours derived from the MCMC analysis for the model parameters k_1 , k_2 and k_3 described in Eq. 11. The left panel is plotted for the rise phase and the right panel is plotted for the decay phase.

C. MCMC PARAMETER PROBABILITY DISTRIBUTIONS

In this section, we show the contour maps and probability distributions for the set of model parameters derived using the MCMC analysis of the relation between the QPO intrinsic rms and frequency. The MCMC analysis is preformed using `emcee` package (Foreman-Mackey et al. 2013), and the contour maps and probability distributions are plotted using `corner` package (Foreman-Mackey 2016). For each map, we show the 0.16, 0.5, and 0.84 quantiles (see Fig. 12).

D. QPO PARAMETERS AND RADIO OBSERVATIONS

In this study, we preform a systematic analysis of type C QPOs with one hundred and six *RXTE*/PCA observational samples of black hole X-ray binary H 1743–322. This source also exhibit significant radio emission, so we take the quasi-simultaneous radio observational results from previously published studies to add to our joint analysis. In this section, we present the QPO parameters of our analysis and the quasi-simultaneous radio flux measurements (if present) at ~ 8.5 GHz. The parameters, QPO frequency (f_{QPO}), full width at half maximum (FWHM), fractional rms amplitude and radio flux density at ~ 8.5 GHz ($S_{\nu=8.5\text{GHz}}$), etc., are presented in Table 2.

Table 2. QPO Parameters and the Quasi-simultaneous Radio Flux Density

ObsID ^a	Outburst Phase ^b	X-ray MJD ^c	f_{QPO}	FWHM ^d	Fractional rms ^e	Radio MJD ^f	$S_{\nu=8.5\text{GHz}}^g$	Notes
			(Hz)	(Hz)	(%)		(mJy)	
80138-01-06-00	Rise	52739.66	$3.22^{+0.01}_{-0.01}$	$0.35^{+0.02}_{-0.02}$	$12.66^{+0.22}_{-0.21}$	52739.46	20.68 ± 0.06	VLA ^h
80138-01-07-00	Rise	52741.83	$7.17^{+0.03}_{-0.03}$	$1.13^{+0.07}_{-0.07}$	$5.49^{+0.13}_{-0.13}$	52741.56	7.71 ± 0.12	VLA ^h
80146-01-01-00	Rise	52743.22	$8.51^{+0.02}_{-0.02}$	$0.56^{+0.04}_{-0.04}$	$3.71^{+0.09}_{-0.09}$	52742.52	3.87 ± 0.13	VLA ^h
80146-01-02-00	Rise	52744.20	$5.62^{+0.02}_{-0.02}$	$0.85^{+0.04}_{-0.04}$	$8.11^{+0.13}_{-0.13}$	52745.43	37.15 ± 0.13	VLA ^h
80146-01-03-00	Rise	52746.18	$4.74^{+0.01}_{-0.01}$	$0.55^{+0.03}_{-0.03}$	$10.52^{+0.22}_{-0.21}$
80146-01-03-01	Rise	52747.61	$7.01^{+0.03}_{-0.03}$	$1.19^{+0.08}_{-0.08}$	$5.52^{+0.14}_{-0.14}$
80146-01-29-00	Rise	52766.56	$5.60^{+0.02}_{-0.02}$	$0.74^{+0.05}_{-0.04}$	$7.87^{+0.15}_{-0.15}$	52765.42	11.12 ± 0.13	VLA ^h
80146-01-30-00	Rise	52767.81	$4.43^{+0.01}_{-0.01}$	$0.53^{+0.02}_{-0.02}$	$10.92^{+0.13}_{-0.13}$	52767.51	23.02 ± 0.12	VLA ^h

Table 2 continued

Table 2 (continued)

ObsID ^a	Outburst Phase ^b	X-ray MJD ^c	f_{QPO}	FWHM ^d	Fractional rms ^e	Radio MJD ^f	$S_{\nu=8.5\text{GHz}}^g$	Notes
			(Hz)	(Hz)	(%)		(mJy)	
80146-01-31-00	Rise	52768.53	$5.41^{+0.02}_{-0.02}$	$0.83^{+0.05}_{-0.05}$	$9.41^{+0.19}_{-0.18}$	52768.49	30.14 ± 0.16	VLA ^h
80146-01-32-00	Rise	52769.72	$4.90^{+0.01}_{-0.01}$	$0.55^{+0.03}_{-0.03}$	$10.74^{+0.23}_{-0.21}$	52769.51	23.80 ± 0.14	VLA ^h
80146-01-33-01	Rise	52770.37	$6.02^{+0.03}_{-0.03}$	$0.85^{+0.07}_{-0.06}$	$7.66^{+0.20}_{-0.20}$
80146-01-33-00	Rise	52770.65	$6.22^{+0.02}_{-0.02}$	$0.85^{+0.06}_{-0.05}$	$7.16^{+0.15}_{-0.15}$
80146-01-34-00	Rise	52771.74	$2.82^{+0.01}_{-0.01}$	$0.33^{+0.02}_{-0.02}$	$13.22^{+0.19}_{-0.17}$
80146-01-35-00	Rise	52771.97	$2.27^{+0.01}_{-0.01}$	$0.19^{+0.03}_{-0.03}$	$12.06^{+0.52}_{-0.52}$
80146-01-36-00	Rise	52772.67	$1.84^{+0.01}_{-0.01}$	$0.25^{+0.01}_{-0.01}$	$13.92^{+0.26}_{-0.26}$
80146-01-37-00	Rise	52773.66	$1.90^{+0.01}_{-0.01}$	$0.26^{+0.02}_{-0.02}$	$13.71^{+0.25}_{-0.25}$	52773.36	35.76 ± 0.23	VLA ^h
80146-01-39-00	Rise	52775.57	$2.15^{+0.01}_{-0.01}$	$0.29^{+0.02}_{-0.02}$	$14.11^{+0.24}_{-0.24}$
80146-01-40-00	Rise	52776.62	$1.72^{+0.01}_{-0.01}$	$0.32^{+0.02}_{-0.02}$	$16.21^{+0.27}_{-0.27}$
80146-01-41-00	Rise	52777.61	$2.50^{+0.01}_{-0.01}$	$0.31^{+0.02}_{-0.02}$	$13.83^{+0.22}_{-0.23}$
80146-01-42-00	Rise	52778.46	$3.21^{+0.01}_{-0.01}$	$0.46^{+0.02}_{-0.02}$	$13.83^{+0.19}_{-0.18}$
80146-01-43-01	Rise	52779.53	$3.82^{+0.02}_{-0.02}$	$0.41^{+0.04}_{-0.03}$	$11.87^{+0.34}_{-0.33}$
80146-01-43-00	Rise	52779.58	$3.81^{+0.01}_{-0.01}$	$0.37^{+0.02}_{-0.02}$	$12.79^{+0.22}_{-0.21}$	52779.44	11.99 ± 0.17	VLA ^h
80146-01-44-00	Rise	52780.57	$3.82^{+0.01}_{-0.01}$	$0.37^{+0.02}_{-0.02}$	$12.59^{+0.22}_{-0.21}$
80146-01-45-00	Rise	52781.55	$3.64^{+0.01}_{-0.01}$	$0.45^{+0.02}_{-0.02}$	$13.31^{+0.18}_{-0.17}$
80146-01-46-00	Rise	52782.67	$4.70^{+0.01}_{-0.01}$	$0.45^{+0.03}_{-0.03}$	$11.18^{+0.21}_{-0.19}$
80146-01-47-00	Rise	52783.46	$6.99^{+0.02}_{-0.02}$	$1.40^{+0.06}_{-0.05}$	$6.13^{+0.10}_{-0.10}$
80146-01-50-00	Rise	52786.29	$9.43^{+0.04}_{-0.04}$	$0.85^{+0.09}_{-0.08}$	$2.09^{+0.08}_{-0.08}$	52786.36	16.06 ± 0.11	VLA ^h
80137-01-25-00	Decay	52937.02	$7.11^{+0.21}_{-0.15}$	$0.91^{+1.51}_{-0.41}$	$6.89^{+1.18}_{-1.17}$	52939.99	0.14 ± 0.04	VLA ^h
80137-01-26-00	Decay	52938.00	$5.93^{+0.44}_{-0.39}$	$1.89^{+1.32}_{-0.77}$	$9.05^{+1.93}_{-1.66}$
80137-02-01-00	Decay	52944.11	$2.48^{+0.15}_{-0.11}$	$0.97^{+0.68}_{-0.38}$	$10.03^{+2.11}_{-1.75}$
93427-01-03-01	Decay	54492.18	$7.03^{+0.10}_{-0.10}$	$0.67^{+0.41}_{-0.26}$	$5.81^{+1.19}_{-0.87}$	54493.32	0.44 ± 0.09	ATCA ⁱ
93427-01-04-00	Decay	54498.84	$3.90^{+0.08}_{-0.08}$	$0.65^{+0.33}_{-0.22}$	$8.00^{+1.71}_{-1.10}$	54499.74	0.52 ± 0.06	VLA ^j
93427-01-04-02	Decay	54500.80	$2.60^{+0.13}_{-0.10}$	$1.50^{+0.82}_{-0.52}$	$13.42^{+1.98}_{-1.77}$	54501.64	0.48 ± 0.08	VLA ^j
93427-01-04-03	Decay	54502.83	$2.36^{+0.14}_{-0.16}$	$0.77^{+0.39}_{-0.35}$	$8.86^{+1.74}_{-1.44}$	54502.56	0.45 ± 0.09	VLA ^j
93427-01-09-00	Rise	54742.98	$0.33^{+0.01}_{-0.01}$	$0.03^{+0.01}_{-0.01}$	$15.19^{+1.68}_{-1.67}$	54744.21	1.74 ± 0.07	ATCA ⁱ
93427-01-09-01	Rise	54746.51	$0.38^{+0.01}_{-0.01}$	$0.03^{+0.01}_{-0.01}$	$15.69^{+0.91}_{-0.89}$
93427-01-09-03	Rise	54747.49	$0.43^{+0.01}_{-0.01}$	$0.03^{+0.01}_{-0.01}$	$15.00^{+0.91}_{-0.89}$	54747.44	2.54 ± 0.08	ATCA ⁱ
93427-01-09-02	Rise	54748.21	$0.47^{+0.01}_{-0.01}$	$0.04^{+0.01}_{-0.01}$	$14.31^{+0.99}_{-0.98}$	54748.44	2.43 ± 0.09	ATCA ⁱ
93427-01-10-00	Rise	54750.37	$0.58^{+0.01}_{-0.01}$	$0.06^{+0.02}_{-0.02}$	$14.19^{+1.31}_{-1.31}$	54749.36	2.38 ± 0.11	ATCA ⁱ
93427-01-10-01	Rise	54752.26	$0.68^{+0.01}_{-0.01}$	$0.07^{+0.01}_{-0.01}$	$15.59^{+0.92}_{-0.91}$
93427-01-10-02	Rise	54755.23	$0.75^{+0.02}_{-0.02}$	$0.12^{+0.03}_{-0.02}$	$13.88^{+1.22}_{-1.24}$
93427-01-11-00	Rise	54756.25	$0.86^{+0.01}_{-0.01}$	$0.10^{+0.01}_{-0.01}$	$15.44^{+0.68}_{-0.67}$
93427-01-11-01	Rise	54758.15	$1.02^{+0.01}_{-0.01}$	$0.12^{+0.02}_{-0.01}$	$14.89^{+0.62}_{-0.62}$
93427-01-11-03	Rise	54762.14	$5.60^{+0.06}_{-0.06}$	$0.49^{+0.23}_{-0.17}$	$5.43^{+0.75}_{-0.66}$
93427-01-12-04	Decay	54767.84	$3.87^{+0.03}_{-0.03}$	$0.47^{+0.09}_{-0.08}$	$10.48^{+0.65}_{-0.62}$
93427-01-12-02	Decay	54768.64	$3.30^{+0.03}_{-0.03}$	$0.35^{+0.09}_{-0.07}$	$11.45^{+0.84}_{-0.81}$
93427-01-12-05	Decay	54769.14	$2.91^{+0.04}_{-0.04}$	$0.38^{+0.10}_{-0.08}$	$12.88^{+1.10}_{-1.05}$
93427-01-13-00	Decay	54770.12	$2.61^{+0.02}_{-0.02}$	$0.42^{+0.06}_{-0.06}$	$12.40^{+0.63}_{-0.61}$
93427-01-13-05	Decay	54770.40	$2.26^{+0.02}_{-0.02}$	$0.25^{+0.05}_{-0.04}$	$11.90^{+0.70}_{-0.68}$
93427-01-13-04	Decay	54771.76	$2.38^{+0.02}_{-0.02}$	$0.29^{+0.05}_{-0.05}$	$11.89^{+0.70}_{-0.68}$
93427-01-13-01	Decay	54772.15	$2.25^{+0.04}_{-0.03}$	$0.36^{+0.15}_{-0.12}$	$12.44^{+1.37}_{-1.27}$
93427-01-13-02	Decay	54773.27	$2.27^{+0.03}_{-0.03}$	$0.33^{+0.08}_{-0.07}$	$12.21^{+0.90}_{-0.86}$
93427-01-13-06	Decay	54774.64	$2.12^{+0.02}_{-0.02}$	$0.38^{+0.07}_{-0.06}$	$12.26^{+0.79}_{-0.75}$	54774.43	0.94 ± 0.12	ATCA ⁱ
93427-01-13-03	Decay	54775.56	$1.83^{+0.03}_{-0.03}$	$0.32^{+0.07}_{-0.06}$	$11.92^{+0.96}_{-0.92}$
93427-01-14-00	Decay	54777.86	$1.89^{+0.04}_{-0.04}$	$0.29^{+0.08}_{-0.07}$	$10.59^{+1.10}_{-1.04}$
93427-01-14-01	Decay	54778.77	$1.82^{+0.04}_{-0.03}$	$0.29^{+0.12}_{-0.09}$	$10.99^{+1.32}_{-1.21}$
93427-01-14-02	Decay	54779.04	$1.52^{+0.02}_{-0.02}$	$0.21^{+0.06}_{-0.05}$	$11.68^{+1.14}_{-1.09}$	54779.35	0.94 ± 0.08	ATCA ⁱ
93427-01-14-03	Decay	54780.02	$1.48^{+0.03}_{-0.03}$	$0.20^{+0.07}_{-0.06}$	$9.89^{+1.22}_{-1.16}$

Table 2 continued

Table 2 (*continued*)

ObsID ^a	Outburst Phase ^b	X-ray MJD ^c	f_{QPO}	FWHM ^d	Fractional rms ^e	Radio MJD ^f	$S_{\nu=8.5\text{GHz}}^g$	Notes
			(Hz)	(Hz)	(%)		(mJy)	
93427-01-14-04	Decay	54781.78	$1.72^{+0.02}_{-0.02}$	$0.17^{+0.07}_{-0.05}$	$9.88^{+1.06}_{-1.01}$
93427-01-14-05	Decay	54782.89	$2.21^{+0.04}_{-0.04}$	$0.32^{+0.10}_{-0.08}$	$11.15^{+1.16}_{-1.11}$
93427-01-14-06	Decay	54783.81	$2.07^{+0.06}_{-0.05}$	$0.42^{+0.20}_{-0.14}$	$11.16^{+1.73}_{-1.44}$
93427-01-15-00	Decay	54784.45	$1.79^{+0.05}_{-0.04}$	$0.26^{+0.12}_{-0.09}$	$9.74^{+1.36}_{-1.22}$
93427-01-15-01	Decay	54785.70	$1.95^{+0.09}_{-0.08}$	$0.52^{+0.27}_{-0.19}$	$10.83^{+2.16}_{-1.74}$
93427-01-15-02	Decay	54786.48	$1.76^{+0.04}_{-0.03}$	$0.28^{+0.11}_{-0.08}$	$9.31^{+1.18}_{-1.07}$
93427-01-15-03	Decay	54787.73	$1.54^{+0.06}_{-0.06}$	$0.27^{+0.16}_{-0.11}$	$9.15^{+1.77}_{-1.57}$
93427-01-15-04	Decay	54788.64	$0.97^{+0.04}_{-0.03}$	$0.18^{+0.14}_{-0.07}$	$9.29^{+2.06}_{-1.67}$
93427-01-15-06	Decay	54788.84	$0.99^{+0.08}_{-0.07}$	$0.23^{+0.19}_{-0.14}$	$8.09^{+2.52}_{-2.08}$
93427-01-15-05	Decay	54789.49	$0.88^{+0.05}_{-0.05}$	$0.22^{+0.24}_{-0.11}$	$8.20^{+2.68}_{-1.82}$
94413-01-02-00	Rise	54980.40	$0.91^{+0.01}_{-0.01}$	$0.04^{+0.01}_{-0.01}$	$17.96^{+0.96}_{-0.96}$	54978.38	2.24 ± 0.03	VLA ^k
94413-01-02-02	Rise	54980.85	$1.00^{+0.01}_{-0.01}$	$0.03^{+0.01}_{-0.01}$	$17.47^{+0.75}_{-0.75}$	54978.38	2.24 ± 0.03	VLA ^k
94413-01-02-01	Rise	54981.95	$1.19^{+0.01}_{-0.01}$	$0.03^{+0.01}_{-0.01}$	$17.16^{+1.08}_{-1.07}$	54981.95	2.73 ± 0.10	VLA ^k
94413-01-02-05	Rise	54982.28	$1.28^{+0.01}_{-0.01}$	$0.04^{+0.01}_{-0.01}$	$17.47^{+0.82}_{-0.81}$
94413-01-02-04	Rise	54983.33	$2.02^{+0.01}_{-0.01}$	$0.09^{+0.01}_{-0.01}$	$17.43^{+0.67}_{-0.66}$
94413-01-02-03	Rise	54984.37	$3.58^{+0.01}_{-0.01}$	$0.33^{+0.04}_{-0.04}$	$14.97^{+1.21}_{-0.69}$	54984.35	1.8 ± 0.3	VLBA ^l
94413-01-07-00	Decay	55016.32	$4.94^{+0.06}_{-0.12}$	$0.26^{+0.45}_{-0.26}$	$6.22^{+2.10}_{-1.46}$
94413-01-07-01	Decay	55019.45	$3.40^{+0.09}_{-0.10}$	$0.39^{+0.29}_{-0.18}$	$7.49^{+2.04}_{-1.54}$	55019.46	0.592 ± 0.055	VLA ^k
94413-01-07-02	Decay	55021.42	$3.81^{+0.17}_{-0.11}$	$0.62^{+0.85}_{-0.29}$	$10.16^{+3.87}_{-2.10}$	55021.42	0.410 ± 0.074	VLA ^k
95405-01-02-06	Decay	55223.39	$3.82^{+0.04}_{-0.04}$	$0.43^{+0.13}_{-0.10}$	$9.55^{+0.91}_{-0.84}$
95405-01-02-02	Decay	55224.67	$3.05^{+0.04}_{-0.04}$	$0.39^{+0.12}_{-0.09}$	$10.54^{+1.04}_{-0.95}$
95405-01-03-00	Decay	55226.53	$2.02^{+0.04}_{-0.03}$	$0.30^{+0.10}_{-0.08}$	$11.23^{+1.19}_{-1.11}$
95405-01-03-04	Decay	55227.77	$2.24^{+0.03}_{-0.04}$	$0.30^{+0.09}_{-0.07}$	$11.36^{+1.12}_{-1.07}$
95405-01-03-01	Decay	55228.61	$2.20^{+0.03}_{-0.03}$	$0.26^{+0.07}_{-0.06}$	$10.21^{+0.89}_{-0.86}$
95405-01-03-05	Decay	55229.54	$1.71^{+0.04}_{-0.04}$	$0.24^{+0.09}_{-0.07}$	$10.10^{+1.31}_{-1.22}$
95405-01-03-02	Decay	55230.59	$1.35^{+0.04}_{-0.04}$	$0.32^{+0.14}_{-0.10}$	$10.75^{+1.62}_{-1.40}$
95405-01-04-01	Decay	55233.40	$0.90^{+0.03}_{-0.03}$	$0.15^{+0.17}_{-0.09}$	$8.15^{+2.44}_{-1.69}$
95360-14-01-00	Rise	55418.41	$1.00^{+0.01}_{-0.01}$	$0.05^{+0.01}_{-0.01}$	$16.56^{+0.60}_{-0.60}$
95360-14-02-01	Rise	55419.09	$1.04^{+0.01}_{-0.01}$	$0.04^{+0.01}_{-0.01}$	$17.38^{+1.46}_{-1.45}$
95360-14-02-00	Rise	55420.23	$1.17^{+0.01}_{-0.01}$	$0.04^{+0.01}_{-0.01}$	$16.66^{+0.61}_{-0.61}$
95360-14-03-00	Rise	55421.28	$1.48^{+0.01}_{-0.01}$	$0.05^{+0.01}_{-0.01}$	$17.02^{+0.64}_{-0.64}$
95360-14-02-03	Rise	55422.02	$1.76^{+0.01}_{-0.01}$	$0.08^{+0.01}_{-0.01}$	$17.30^{+0.89}_{-0.89}$
95360-14-02-02	Rise	55423.20	$2.96^{+0.02}_{-0.01}$	$0.20^{+0.04}_{-0.03}$	$14.88^{+0.87}_{-0.80}$
95360-14-03-01	Rise	55424.06	$4.80^{+0.04}_{-0.04}$	$0.37^{+0.09}_{-0.07}$	$9.44^{+0.71}_{-0.70}$
95360-14-23-00	Decay	55456.67	$3.34^{+0.08}_{-0.07}$	$0.58^{+0.38}_{-0.22}$	$11.00^{+2.30}_{-1.77}$
95360-14-23-01	Decay	55457.12	$2.57^{+0.05}_{-0.04}$	$0.25^{+0.18}_{-0.11}$	$9.34^{+1.77}_{-1.47}$
96425-01-01-00	Rise	55663.67	$0.43^{+0.01}_{-0.01}$	$0.03^{+0.01}_{-0.01}$	$14.61^{+0.88}_{-0.87}$
96425-01-02-00	Rise	55667.59	$0.67^{+0.01}_{-0.01}$	$0.05^{+0.01}_{-0.01}$	$15.72^{+0.54}_{-0.53}$
96425-01-02-01	Rise	55668.98	$0.89^{+0.01}_{-0.01}$	$0.08^{+0.02}_{-0.01}$	$16.05^{+0.99}_{-0.96}$
96425-01-02-02	Rise	55670.62	$1.36^{+0.01}_{-0.01}$	$0.14^{+0.01}_{-0.01}$	$15.80^{+0.53}_{-0.52}$
96425-01-02-05	Rise	55671.53	$1.82^{+0.01}_{-0.01}$	$0.21^{+0.03}_{-0.03}$	$15.61^{+0.67}_{-0.67}$
96425-01-02-03	Rise	55672.84	$3.61^{+0.03}_{-0.03}$	$0.29^{+0.07}_{-0.06}$	$12.21^{+0.87}_{-0.86}$
96425-01-05-01	Decay	55690.13	$2.98^{+0.07}_{-0.07}$	$0.54^{+0.27}_{-0.17}$	$10.99^{+1.49}_{-1.35}$
96425-01-05-02	Decay	55691.51	$2.01^{+0.03}_{-0.03}$	$0.24^{+0.16}_{-0.11}$	$11.00^{+1.51}_{-1.31}$
96425-01-05-03	Decay	55693.00	$1.81^{+0.04}_{-0.04}$	$0.28^{+0.14}_{-0.10}$	$10.88^{+1.47}_{-1.34}$
96425-01-06-00	Decay	55694.00	$1.47^{+0.04}_{-0.03}$	$0.24^{+0.16}_{-0.11}$	$9.48^{+1.59}_{-1.39}$
96425-01-06-01	Decay	55695.42	$1.20^{+0.04}_{-0.04}$	$0.19^{+0.14}_{-0.08}$	$8.43^{+1.64}_{-1.47}$

Table 2 *continued*

Table 2 (continued)

ObsID ^a	Outburst Phase ^b	X-ray MJD ^c	f_{QPO}	FWHM ^d	Fractional rms ^e	Radio MJD ^f	$S_{\nu=8.5\text{GHz}}^g$	Notes
			(Hz)	(Hz)	(%)		(mJy)	

NOTE—^a Observational ID of *RXTE* data. ^b Outburst phase (rise phase or decay phase). ^c Modified Julian Day of the *RXTE* observation. ^d Full width at half maximum of the QPO. ^e The QPO fractional rms calculated by Eq. 1. ^f Modified Julian Day of the radio observation. ^g The radio flux density at ~ 8.5 GHz. ^h The radio flux measurements of Very Large Array (VLA) are taken from McClintock et al. (2009). ⁱ The radio flux measurements of Australia Telescope Compact Array (ATCA) are taken from Coriat et al. (2011). ^j The radio flux measurements of Very Large Array (VLA) are taken from Jonker et al. (2010). ^k The radio flux measurements of Very Large Array (VLA) are taken from Coriat et al. (2011). ^l The radio flux measurements of Very Long Baseline Array (VLBA) are taken from Miller-Jones et al. (2012).

REFERENCES

- Aneesha, U., & Mandal, S. 2020, *A&A*, 637, A47, doi: [10.1051/0004-6361/202037577](https://doi.org/10.1051/0004-6361/202037577)
- Aneesha, U., Mandal, S., & Sreehari, H. 2019, *MNRAS*, 486, 2705, doi: [10.1093/mnras/stz1000](https://doi.org/10.1093/mnras/stz1000)
- Axelsson, M., & Done, C. 2016, *MNRAS*, 458, 1778, doi: [10.1093/mnras/stw464](https://doi.org/10.1093/mnras/stw464)
- Axelsson, M., Hjalmarsdotter, L., & Done, C. 2013, *MNRAS*, 431, 1987, doi: [10.1093/mnras/stt315](https://doi.org/10.1093/mnras/stt315)
- Band, D. L., & Grindlay, J. E. 1986, *ApJ*, 311, 595, doi: [10.1086/164799](https://doi.org/10.1086/164799)
- Bellavita, C., García, F., Méndez, M., & Karpouzas, K. 2022, *MNRAS*, 515, 2099, doi: [10.1093/mnras/stac1922](https://doi.org/10.1093/mnras/stac1922)
- Belloni, T., & Hasinger, G. 1990, *A&A*, 230, 103
- Belloni, T., Homan, J., Casella, P., et al. 2005, *A&A*, 440, 207, doi: [10.1051/0004-6361:20042457](https://doi.org/10.1051/0004-6361:20042457)
- Bhattacharjee, A., Banerjee, I., Banerjee, A., Debnath, D., & Chakrabarti, S. K. 2017, *MNRAS*, 466, 1372, doi: [10.1093/mnras/stw3117](https://doi.org/10.1093/mnras/stw3117)
- Bisnovatyi-Kogan, G. S., & Blinnikov, S. I. 1976, *Soviet Astronomy Letters*, 2, 191. <https://arxiv.org/abs/astro-ph/0003275>
- Blandford, R. D., & Königl, A. 1979, *ApJ*, 232, 34, doi: [10.1086/157262](https://doi.org/10.1086/157262)
- Bu, Q.-c., Chen, L., Li, Z.-s., et al. 2015, *ApJ*, 799, 2, doi: [10.1088/0004-637X/799/1/2](https://doi.org/10.1088/0004-637X/799/1/2)
- Capitanio, F., Belloni, T., Del Santo, M., & Ubertini, P. 2009, *MNRAS*, 398, 1194, doi: [10.1111/j.1365-2966.2009.15196.x](https://doi.org/10.1111/j.1365-2966.2009.15196.x)
- Casella, P., Belloni, T., & Stella, L. 2005, *ApJ*, 629, 403, doi: [10.1086/431174](https://doi.org/10.1086/431174)
- Chand, S., Agrawal, V. K., Dewangan, G. C., Tripathi, P., & Thakur, P. 2020, *ApJ*, 893, 142, doi: [10.3847/1538-4357/ab829a](https://doi.org/10.3847/1538-4357/ab829a)
- Chen, Y. P., Zhang, S., Torres, D. F., et al. 2010, *A&A*, 522, A99, doi: [10.1051/0004-6361/201014017](https://doi.org/10.1051/0004-6361/201014017)
- Coriat, M., Corbel, S., Prat, L., et al. 2011, *MNRAS*, 414, 677, doi: [10.1111/j.1365-2966.2011.18433.x](https://doi.org/10.1111/j.1365-2966.2011.18433.x)
- Dauser, T., Garcia, J., Parker, M. L., Fabian, A. C., & Wilms, J. 2014, *MNRAS*, 444, L100, doi: [10.1093/mnrasl/slu125](https://doi.org/10.1093/mnrasl/slu125)
- Dauser, T., Wilms, J., Reynolds, C. S., & Brenneman, L. W. 2010, *MNRAS*, 409, 1534, doi: [10.1111/j.1365-2966.2010.17393.x](https://doi.org/10.1111/j.1365-2966.2010.17393.x)
- Done, C., Gierliński, M., & Kubota, A. 2007, *A&A Rv*, 15, 1, doi: [10.1007/s00159-007-0006-1](https://doi.org/10.1007/s00159-007-0006-1)
- Esin, A. A., McClintock, J. E., & Narayan, R. 1997, *ApJ*, 489, 865, doi: [10.1086/304829](https://doi.org/10.1086/304829)
- Fabian, A. C., Rees, M. J., Stella, L., & White, N. E. 1989, *MNRAS*, 238, 729, doi: [10.1093/mnras/238.3.729](https://doi.org/10.1093/mnras/238.3.729)
- Fender, R., & Belloni, T. 2004, *ARA&A*, 42, 317, doi: [10.1146/annurev.astro.42.053102.134031](https://doi.org/10.1146/annurev.astro.42.053102.134031)
- Fender, R. P. 2001, *MNRAS*, 322, 31, doi: [10.1046/j.1365-8711.2001.04080.x](https://doi.org/10.1046/j.1365-8711.2001.04080.x)
- Fender, R. P., Belloni, T. M., & Gallo, E. 2004, *MNRAS*, 355, 1105, doi: [10.1111/j.1365-2966.2004.08384.x](https://doi.org/10.1111/j.1365-2966.2004.08384.x)
- Fender, R. P., Homan, J., & Belloni, T. M. 2009, *MNRAS*, 396, 1370, doi: [10.1111/j.1365-2966.2009.14841.x](https://doi.org/10.1111/j.1365-2966.2009.14841.x)
- Foreman-Mackey, D. 2016, *The Journal of Open Source Software*, 1, 24, doi: [10.21105/joss.00024](https://doi.org/10.21105/joss.00024)
- Foreman-Mackey, D., Hogg, D. W., Lang, D., & Goodman, J. 2013, *PASP*, 125, 306, doi: [10.1086/670067](https://doi.org/10.1086/670067)
- García, F., Karpouzas, K., Méndez, M., et al. 2022, *MNRAS*, 513, 4196, doi: [10.1093/mnras/stac1202](https://doi.org/10.1093/mnras/stac1202)
- García, F., Méndez, M., Karpouzas, K., et al. 2021, *MNRAS*, 501, 3173, doi: [10.1093/mnras/staa3944](https://doi.org/10.1093/mnras/staa3944)
- García, J., Dauser, T., Reynolds, C. S., et al. 2013, *ApJ*, 768, 146, doi: [10.1088/0004-637X/768/2/146](https://doi.org/10.1088/0004-637X/768/2/146)
- García, J., Dauser, T., Lohfink, A., et al. 2014, *ApJ*, 782, 76, doi: [10.1088/0004-637X/782/2/76](https://doi.org/10.1088/0004-637X/782/2/76)
- García, J. A., Dauser, T., Steiner, J. F., et al. 2015a, *ApJL*, 808, L37, doi: [10.1088/2041-8205/808/2/L37](https://doi.org/10.1088/2041-8205/808/2/L37)

- García, J. A., Steiner, J. F., McClintock, J. E., et al. 2015b, *ApJ*, 813, 84, doi: [10.1088/0004-637X/813/2/84](https://doi.org/10.1088/0004-637X/813/2/84)
- Georganopoulos, M., Aharonian, F. A., & Kirk, J. G. 2002, *A&A*, 388, L25, doi: [10.1051/0004-6361:20020567](https://doi.org/10.1051/0004-6361:20020567)
- Homan, J., & Belloni, T. 2005, *Ap&SS*, 300, 107, doi: [10.1007/s10509-005-1197-4](https://doi.org/10.1007/s10509-005-1197-4)
- Homan, J., Miller, J. M., Wijnands, R., et al. 2005, *ApJ*, 623, 383, doi: [10.1086/424994](https://doi.org/10.1086/424994)
- Homan, J., Wijnands, R., van der Klis, M., et al. 2001, *ApJS*, 132, 377, doi: [10.1086/318954](https://doi.org/10.1086/318954)
- Huang, Y., Qu, J. L., Zhang, S. N., et al. 2018, *ApJ*, 866, 122, doi: [10.3847/1538-4357/aade4c](https://doi.org/10.3847/1538-4357/aade4c)
- Ingram, A., Done, C., & Fragile, P. C. 2009, *MNRAS*, 397, L101, doi: [10.1111/j.1745-3933.2009.00693.x](https://doi.org/10.1111/j.1745-3933.2009.00693.x)
- Ingram, A., Maccarone, T. J., Poutanen, J., & Krawczynski, H. 2015, *ApJ*, 807, 53, doi: [10.1088/0004-637X/807/1/53](https://doi.org/10.1088/0004-637X/807/1/53)
- Ingram, A., & van der Klis, M. 2015, *MNRAS*, 446, 3516, doi: [10.1093/mnras/stu2373](https://doi.org/10.1093/mnras/stu2373)
- Ingram, A., van der Klis, M., Middleton, M., Altamirano, D., & Uttley, P. 2017, *MNRAS*, 464, 2979, doi: [10.1093/mnras/stw2581](https://doi.org/10.1093/mnras/stw2581)
- Ingram, A., van der Klis, M., Middleton, M., et al. 2016, *MNRAS*, 461, 1967, doi: [10.1093/mnras/stw1245](https://doi.org/10.1093/mnras/stw1245)
- Ingram, A. R., & Motta, S. E. 2019, *NewAR*, 85, 101524, doi: [10.1016/j.newar.2020.101524](https://doi.org/10.1016/j.newar.2020.101524)
- Jonker, P. G., Miller-Jones, J., Homan, J., et al. 2010, *MNRAS*, 401, 1255, doi: [10.1111/j.1365-2966.2009.15717.x](https://doi.org/10.1111/j.1365-2966.2009.15717.x)
- Kaluzienski, L. J., & Holt, S. S. 1977, *IAUC*, 3099, 3
- Kara, E., Steiner, J. F., Fabian, A. C., et al. 2019, *Nature*, 565, 198, doi: [10.1038/s41586-018-0803-x](https://doi.org/10.1038/s41586-018-0803-x)
- Karpouzas, K., Méndez, M., García, F., et al. 2021, *MNRAS*, 503, 5522, doi: [10.1093/mnras/stab827](https://doi.org/10.1093/mnras/stab827)
- Karpouzas, K., Méndez, M., Ribeiro, E. M., et al. 2020, *MNRAS*, 492, 1399, doi: [10.1093/mnras/stz3502](https://doi.org/10.1093/mnras/stz3502)
- Kato, S. 1990, *PASJ*, 42, 99
- Kong, L. D., Zhang, S., Chen, Y. P., et al. 2020, *Journal of High Energy Astrophysics*, 25, 29, doi: [10.1016/j.jheap.2020.01.003](https://doi.org/10.1016/j.jheap.2020.01.003)
- Kumar, N., & Misra, R. 2014, *MNRAS*, 445, 2818, doi: [10.1093/mnras/stu1946](https://doi.org/10.1093/mnras/stu1946)
- Lee, H. C., & Miller, G. S. 1998, *MNRAS*, 299, 479, doi: [10.1046/j.1365-8711.1998.01842.x](https://doi.org/10.1046/j.1365-8711.1998.01842.x)
- Liu, B. F., & Qiao, E. 2022, *arXiv e-prints*, arXiv:2201.06198. <https://arxiv.org/abs/2201.06198>
- Lynden-Bell, D., & Pringle, J. E. 1974, *MNRAS*, 168, 603, doi: [10.1093/mnras/168.3.603](https://doi.org/10.1093/mnras/168.3.603)
- Maccarone, T. J. 2003, *A&A*, 409, 697, doi: [10.1051/0004-6361:20031146](https://doi.org/10.1051/0004-6361:20031146)
- Malzac, J., Merloni, A., & Fabian, A. C. 2004, *MNRAS*, 351, 253, doi: [10.1111/j.1365-2966.2004.07772.x](https://doi.org/10.1111/j.1365-2966.2004.07772.x)
- Markoff, S., Nowak, M. A., & Wilms, J. 2005, *ApJ*, 635, 1203, doi: [10.1086/497628](https://doi.org/10.1086/497628)
- Mastichiadis, A., Petropoulou, M., & Kylafis, N. D. 2022, *A&A*, 662, A118, doi: [10.1051/0004-6361/202243397](https://doi.org/10.1051/0004-6361/202243397)
- McClintock, J. E., Remillard, R. A., Rupen, M. P., et al. 2009, *ApJ*, 698, 1398, doi: [10.1088/0004-637X/698/2/1398](https://doi.org/10.1088/0004-637X/698/2/1398)
- Méndez, M., Karpouzas, K., García, F., et al. 2022, *Nature Astronomy*, 6, 577, doi: [10.1038/s41550-022-01617-y](https://doi.org/10.1038/s41550-022-01617-y)
- Merloni, A., & Fabian, A. C. 2001, *MNRAS*, 321, 549, doi: [10.1046/j.1365-8711.2001.04060.x](https://doi.org/10.1046/j.1365-8711.2001.04060.x)
- Miller, J. M., Raymond, J., Homan, J., et al. 2006, *ApJ*, 646, 394, doi: [10.1086/504673](https://doi.org/10.1086/504673)
- Miller-Jones, J. C. A., Sivakoff, G. R., Altamirano, D., et al. 2012, *MNRAS*, 421, 468, doi: [10.1111/j.1365-2966.2011.20326.x](https://doi.org/10.1111/j.1365-2966.2011.20326.x)
- Miyamoto, S., Kimura, K., Kitamoto, S., Dotani, T., & Ebisawa, K. 1991, *ApJ*, 383, 784, doi: [10.1086/170837](https://doi.org/10.1086/170837)
- Molteni, D., Sponholz, H., & Chakrabarti, S. K. 1996, *ApJ*, 457, 805, doi: [10.1086/176775](https://doi.org/10.1086/176775)
- Motta, S., Muñoz-Darias, T., & Belloni, T. 2010, *MNRAS*, 408, 1796, doi: [10.1111/j.1365-2966.2010.17246.x](https://doi.org/10.1111/j.1365-2966.2010.17246.x)
- Motta, S. E., Casella, P., Henze, M., et al. 2015, *MNRAS*, 447, 2059, doi: [10.1093/mnras/stu2579](https://doi.org/10.1093/mnras/stu2579)
- Narayan, R., & Yi, I. 1994, *ApJL*, 428, L13, doi: [10.1086/187381](https://doi.org/10.1086/187381)
- Nathan, E., Ingram, A., Homan, J., et al. 2022, *MNRAS*, 511, 255, doi: [10.1093/mnras/stab3803](https://doi.org/10.1093/mnras/stab3803)
- Parmar, A. N., Kuulkers, E., Oosterbroek, T., et al. 2003, *A&A*, 411, L421, doi: [10.1051/0004-6361:20031140](https://doi.org/10.1051/0004-6361:20031140)
- Plant, D. S., Fender, R. P., Ponti, G., Muñoz-Darias, T., & Coriat, M. 2014, *MNRAS*, 442, 1767, doi: [10.1093/mnras/stu867](https://doi.org/10.1093/mnras/stu867)
- Reig, P., & Kylafis, N. D. 2021, *A&A*, 646, A112, doi: [10.1051/0004-6361/202039903](https://doi.org/10.1051/0004-6361/202039903)
- Remillard, R. A., & McClintock, J. E. 2006, *ARA&A*, 44, 49, doi: [10.1146/annurev.astro.44.051905.092532](https://doi.org/10.1146/annurev.astro.44.051905.092532)
- Shakura, N. I., & Sunyaev, R. A. 1973, *A&A*, 24, 337
- Shidatsu, M., Ueda, Y., Yamada, S., et al. 2014, *ApJ*, 789, 100, doi: [10.1088/0004-637X/789/2/100](https://doi.org/10.1088/0004-637X/789/2/100)
- Shui, Q. C., Yin, H. X., Zhang, S., et al. 2021, *MNRAS*, 508, 287, doi: [10.1093/mnras/stab2521](https://doi.org/10.1093/mnras/stab2521)
- Smith, A., Kaaret, P., Holder, J., et al. 2009, *ApJ*, 693, 1621, doi: [10.1088/0004-637X/693/2/1621](https://doi.org/10.1088/0004-637X/693/2/1621)
- Sobolewska, M. A., & Życki, P. T. 2006, *MNRAS*, 370, 405, doi: [10.1111/j.1365-2966.2006.10489.x](https://doi.org/10.1111/j.1365-2966.2006.10489.x)
- Steiner, J. F., McClintock, J. E., & Reid, M. J. 2012, *ApJL*, 745, L7, doi: [10.1088/2041-8205/745/1/L7](https://doi.org/10.1088/2041-8205/745/1/L7)

- Stella, L., & Vietri, M. 1998, *ApJL*, 492, L59,
doi: [10.1086/311075](https://doi.org/10.1086/311075)
- Stella, L., Vietri, M., & Morsink, S. M. 1999, *ApJL*, 524, L63, doi: [10.1086/312291](https://doi.org/10.1086/312291)
- Stiele, H., & Yu, W. 2016, *MNRAS*, 460, 1946,
doi: [10.1093/mnras/stw821](https://doi.org/10.1093/mnras/stw821)
- Sunyaev, R. A., & Titarchuk, L. G. 1980, *A&A*, 86, 121
- Tagger, M., & Pellat, R. 1999, *A&A*, 349, 1003.
<https://arxiv.org/abs/astro-ph/9907267>
- Titarchuk, L. 1994, *ApJ*, 434, 570, doi: [10.1086/174760](https://doi.org/10.1086/174760)
- Uttley, P., Wilkinson, T., Cassatella, P., et al. 2011, *MNRAS*, 414, L60, doi: [10.1111/j.1745-3933.2011.01056.x](https://doi.org/10.1111/j.1745-3933.2011.01056.x)
- van den Eijnden, J., Ingram, A., Uttley, P., et al. 2017, *MNRAS*, 464, 2643, doi: [10.1093/mnras/stw2634](https://doi.org/10.1093/mnras/stw2634)
- van der Klis, M. 1989, *ARA&A*, 27, 517,
doi: [10.1146/annurev.aa.27.090189.002505](https://doi.org/10.1146/annurev.aa.27.090189.002505)
- van Doesburgh, M., & van der Klis, M. 2020, *MNRAS*, 496, 5262, doi: [10.1093/mnras/staa1867](https://doi.org/10.1093/mnras/staa1867)
- Veledina, A., Poutanen, J., & Ingram, A. 2013, *ApJ*, 778, 165, doi: [10.1088/0004-637X/778/2/165](https://doi.org/10.1088/0004-637X/778/2/165)
- Wagoner, R. V. 1999, *PhR*, 311, 259,
doi: [10.1016/S0370-1573\(98\)00104-5](https://doi.org/10.1016/S0370-1573(98)00104-5)
- Wang, P. J., Kong, L. D., Chen, Y. P., et al. 2022, *MNRAS*, 512, 4541, doi: [10.1093/mnras/stac773](https://doi.org/10.1093/mnras/stac773)
- Weng, S.-S., Cai, Z.-Y., Zhang, S.-N., et al. 2021, *ApJL*, 915, L15, doi: [10.3847/2041-8213/ac0a7b](https://doi.org/10.3847/2041-8213/ac0a7b)
- Wijnands, R., Homan, J., & van der Klis, M. 1999, *ApJL*, 526, L33, doi: [10.1086/312365](https://doi.org/10.1086/312365)
- Williams, D. R. A., Motta, S. E., Fender, R., et al. 2020, *MNRAS*, 491, L29, doi: [10.1093/mnrasl/slz152](https://doi.org/10.1093/mnrasl/slz152)
- Wilms, J., Allen, A., & McCray, R. 2000, *ApJ*, 542, 914,
doi: [10.1086/317016](https://doi.org/10.1086/317016)
- You, B., Bursa, M., & Życki, P. T. 2018, *ApJ*, 858, 82,
doi: [10.3847/1538-4357/aabd33](https://doi.org/10.3847/1538-4357/aabd33)
- You, B., Życki, P. T., Ingram, A., Bursa, M., & Wang, W. 2020, *ApJ*, 897, 27, doi: [10.3847/1538-4357/ab9838](https://doi.org/10.3847/1538-4357/ab9838)
- You, B., Tuo, Y., Li, C., et al. 2021, *Nature Communications*, 12, 1025,
doi: [10.1038/s41467-021-21169-5](https://doi.org/10.1038/s41467-021-21169-5)
- Yuan, F., & Narayan, R. 2014, *ARA&A*, 52, 529,
doi: [10.1146/annurev-astro-082812-141003](https://doi.org/10.1146/annurev-astro-082812-141003)
- Zdziarski, A. A., Gierliński, M., Mikołajewska, J., et al. 2004, *MNRAS*, 351, 791,
doi: [10.1111/j.1365-2966.2004.07830.x](https://doi.org/10.1111/j.1365-2966.2004.07830.x)
- Zdziarski, A. A., Johnson, W. N., & Magdziarz, P. 1996, *MNRAS*, 283, 193, doi: [10.1093/mnras/283.1.193](https://doi.org/10.1093/mnras/283.1.193)
- Zdziarski, A. A., Lubiński, P., & Smith, D. A. 1999, *MNRAS*, 303, L11, doi: [10.1046/j.1365-8711.1999.02343.x](https://doi.org/10.1046/j.1365-8711.1999.02343.x)
- Zhang, L., Wang, Y., Méndez, M., et al. 2017, *ApJ*, 845, 143, doi: [10.3847/1538-4357/aa8138](https://doi.org/10.3847/1538-4357/aa8138)
- Zhang, L., Méndez, M., Altamirano, D., et al. 2020, *MNRAS*, 494, 1375, doi: [10.1093/mnras/staa797](https://doi.org/10.1093/mnras/staa797)
- Zhang, Y., Méndez, M., García, F., et al. 2022, *MNRAS*, 512, 2686, doi: [10.1093/mnras/stac690](https://doi.org/10.1093/mnras/stac690)
- Zhou, J. N., Liu, Q. Z., Chen, Y. P., et al. 2013, *MNRAS*, 431, 2285, doi: [10.1093/mnras/stt326](https://doi.org/10.1093/mnras/stt326)
- Życki, P. T., Done, C., & Smith, D. A. 1999, *MNRAS*, 309, 561, doi: [10.1046/j.1365-8711.1999.02885.x](https://doi.org/10.1046/j.1365-8711.1999.02885.x)